




## Article

# Targeting Ultrasmall Gold Nanoparticles with cRGD Peptide Increases the Uptake and Efficacy of Cytotoxic Payload

Richard D. Perrins <sup>1,†</sup>, Lee-Anne McCarthy <sup>2,†</sup>, Angela Robinson <sup>1,†</sup>, Kelly L. Spry <sup>1</sup>, Valentin Cognet <sup>1</sup>, Avelino Ferreira <sup>1,‡</sup>, John Porter <sup>1</sup>, Cristina Espinosa García <sup>1</sup>, Miguel Ángel Rodríguez <sup>1</sup>, Diana Lopez <sup>1</sup>, Ibon Perera <sup>1</sup> , Kelly Conlon <sup>1</sup>, Africa Barrientos <sup>1</sup>, Tom Coulter <sup>1</sup>, Alessandro Pace <sup>1</sup>, Sarah J. M. Hale <sup>1</sup>, Enrico Ferrari <sup>2</sup>  and Csanad Z. Bachrati <sup>2,\*</sup> 

<sup>1</sup> Midatech Pharma Plc, 1 Caspian Point, Caspian Way, Cardiff CF10 4DQ, UK

<sup>2</sup> School of Life Sciences, University of Lincoln, Joseph Banks Laboratories, Green Lane, Lincoln LN6 7DL, UK

\* Correspondence: cbachrati@lincoln.ac.uk; Tel.: +44-1522-886787

† These authors contributed equally to this work.

‡ Present address: Department of Chemistry, Royal College of Surgeons in Ireland (RCSI), Dublin D02 YN77, Ireland.

**Abstract:** Cyclic arginyl-glycyl-aspartic acid peptide (cRGD) peptides show a high affinity towards  $\alpha V\beta 3$  integrin, a receptor overexpressed in many cancers. We aimed to combine the versatility of ultrasmall gold nanoparticles (usGNP) with the target selectivity of cRGD peptide for the directed delivery of a cytotoxic payload in a novel design. usGNPs were synthesized with a modified Brust-Schiffrin method and functionalized via amide coupling and ligand exchange and their uptake, intracellular trafficking, and toxicity were characterized. Our cRGD functionalized usGNPs demonstrated increased cellular uptake by  $\alpha V\beta 3$  integrin expressing cells, are internalized via clathrin-dependent endocytosis, accumulated in the lysosomes, and when loaded with mertansine led to increased cytotoxicity. Targeting via cRGD functionalization provides a mechanism to improve the efficacy, tolerability, and retention of therapeutic GNPs.

**Keywords:** ultra-small gold nanoparticles; DM1; cRGD-peptide;  $\alpha V\beta 3$  integrin; targeted drug delivery



**Citation:** Perrins, R.D.; McCarthy, L.-A.; Robinson, A.; Spry, K.L.; Cognet, V.; Ferreira, A.; Porter, J.; García, C.E.; Rodríguez, M.Á.; Lopez, D.; et al. Targeting Ultrasmall Gold Nanoparticles with cRGD Peptide Increases the Uptake and Efficacy of Cytotoxic Payload. *Nanomaterials* **2022**, *12*, 4013. <https://doi.org/10.3390/nano12224013>

Academic Editor: Sónia Carabineiro

Received: 19 October 2022

Accepted: 14 November 2022

Published: 15 November 2022

**Publisher's Note:** MDPI stays neutral with regard to jurisdictional claims in published maps and institutional affiliations.



**Copyright:** © 2022 by the authors. Licensee MDPI, Basel, Switzerland. This article is an open access article distributed under the terms and conditions of the Creative Commons Attribution (CC BY) license (<https://creativecommons.org/licenses/by/4.0/>).

## 1. Introduction

Gold nanoparticles (GNPs) provide a useful scaffold to which a variety of different ligands may be attached to imbue desirable properties such as improved solubility, stability, stealth, delivering a therapeutic payload or targeting the GNP to a specific cell type or location through passive mechanisms (by enhanced permeability and retention effect) or active delivery (using a ligand specific to a tissue or a cell type) [1,2]. Targeting may lead to improved biodistribution, reduced drug degradation, prevention of off-target effects, and thereby increasing the therapeutic window [3]. The cyclic-peptide cRGD is a well-characterized integrin-binding ligand that has previously been used to redirect drugs [4], polydopamine nanoparticles [5], iron oxide nanoparticles [6], virus-derived particles [7], fluorescent polymer nanoparticles [8] to cells that express RGD motif interacting integrins:  $\alpha 8\beta 1$ ,  $\alpha V\beta 3$ ,  $\alpha V\beta 5$ ,  $\alpha V\beta 6$ ,  $\alpha V\beta 8$ , and  $\alpha IIb\beta 3$  [9,10]. Several studies designed for in vitro and in vivo cancer cell imaging have confirmed the potential of such functionalized GNPs [11–14] and called for further characterization and development.

Composed of an inert gold core, GNPs are not expected to have cytotoxicity; consequently, in vivo toxicity data of GNPs is limited [15–17]. usGNPs are mainly cleared through the kidneys [18–20], while those particles that are not cleared accumulate in organs rich in elements of the mononuclear phagocyte system (MPS) such as the liver and spleen [20–22]. The core size was shown to affect systemic toxicity in vivo [17], however, surface charge and functionalization are thought to contribute more significantly to cytotoxicity [23–26].

Ultrasmall GNPs offer several advantages compared to GNPs with sizes over 10 nm. usGNPs have an improved surface/volume ratio, which allows the immobilization of larger amounts of payload at the same dose of gold. They have improved penetration and retention in tumors and fast clearance in normal tissues [27,28]. Similar to the long-recognized suitability of GNPs for delivering cytotoxic payload [29], such potential of usGNPs is also promising; delivery of drugs such as daunorubicin [30], gemcitabine [31], 6-mercaptopurine [32], dodecylcysteine [33], 5-fluorouracil [34], cisplatin [35,36], and doxorubicin [37] have been confirmed. Small GNPs also show greater X-ray attenuation than their larger counterparts, making them better suited as a base for CT contrast agents [38,39]. Furthermore, usGNPs proved to be a suitable nanocarrier for nuclear delivery, with a cut-off size of <10 nm to penetrate the nuclear pores [40]. Besides biocompatibility and tunable functionalization, the size of GNPs can be precisely controlled [41], thus providing an ideal platform to develop multi-functional nanocarriers with effective uptake into tissues, cells, and sub-cellular compartments.

In this study, we present evidence for specific, high-affinity physical interaction between cRGD-functionalized usGNPs and  $\alpha V\beta 3$  integrin *in vitro*, which mediates a selective uptake by cells that express  $\alpha V\beta 3$  integrin. We provide evidence that our cRGD-functionalized usGNPs are internalized via the clathrin-dependent endocytosis pathway and accumulate in the endosomes. We generated cytotoxic usGNPs by attaching mertansine (DM1), a tubulin polymerization inhibitor maytansinoid drug to the cRGD functionalized usGNPs. DM1 can be attached to usGNPs through its thiol group, is released via ligand exchange with intracellular reduced thiols such as glutathione [42], and has been commercialized in an antibody-drug conjugate therapy (Ado-trastuzumab emtansine, Kadcyla<sup>TM</sup>) [43]. Our data provide evidence that usGNPs functionalized with cRGD and DM1 are selectively cytotoxic to cells that express  $\alpha V\beta 3$  integrin and highlight the potential of the platform for the targeted delivery of therapeutic payloads, warranting further preclinical evaluation.

## 2. Materials and Methods

### 2.1. Base GNP Synthesis

Synthesis was performed with a modified Brust-Schiffrin method, using a Atlas Potassium reactor (Syrris Ltd., Royston, United Kingdom) with a 2 L jacketed torispherical vessel and a 500–50 mm blade propeller stirrer. The reaction was carried out at 18 °C with fast stirring (750 rpm). Time, pH, and temperature were continuously monitored. H<sub>2</sub>O (Ultrapure, MilliQ; MilliporeSigma, Burlington, VT, USA) was the solvent used for both synthesis and purification. The different reagents were added from the top of the vessel within minutes (~15 min) using a 150–80–8 mm funnel starting with HAuCl<sub>4</sub>•3H<sub>2</sub>O (1 equivalent, 400 mg, 1.016 mmol, 1645 mL; Sigma-Aldrich, St. Louis, MI, USA). Aqueous NaOH solution (~3 mL 2 M NaOH, Sigma-Aldrich) was used to modulate the pH to ~11.0. Freshly prepared NaBH<sub>4</sub> in excess (0.2 M in 0.01 M NaOH, five equivalents, 192 mg, 5.078 mmol, 25 mL; AppliChem GmbH, Darmstadt, Germany) was quickly added to initiate the nucleation of the particles. Five seconds after nucleation, a 20 mL solution containing the disulfide ligands  $\alpha$ -Thio- $\omega$ -(propionic acid) octa (ethylene glycol) (0.129 equivalent, 118 mg, 0.129 mmol, 10 mL; Acadechem Company Ltd., Hong Kong) and 2'-Thioethyl  $\alpha$ -D-galactopyranoside (0.023 equivalent, 11 mg, 0.023 mmol, 10 mL; GalChimia, A Coruña, Spain) was added in an 85:15 molar ratio. Thirty seconds after nucleation, extra aqueous NaOH solution (~7 mL 2 M NaOH) was used to adjust the pH to ~12. After all reagents were added, the stirring speed was dropped to 550 rpm and the reaction was left to incubate for 30 min. The gold concentration was 0.6 mM and the final volume of the reaction corresponded to 85% of the reactor capacity. Purification was performed with a KR2i TFF system (Repligen, Waltham, MA, USA) using a hollow fiber filter with a 10 kDa molecular weight cut-off. The final product was filtered with a 0.22  $\mu$ m membrane and resuspended in H<sub>2</sub>O at a final target gold concentration of 4 mg/mL.

## 2.2. Functionalization of GNPs

### 2.2.1. Ligand Exchange of DM1 onto GNP

Base GNP (15 mg Au) was solvent exchanged into 38% (*v/v*) DMSO/H<sub>2</sub>O using 10 kDa Amicon 15-Ultra filters (MilliporeSigma) to achieve a final gold concentration of 1 mg/mL. To the 15 mL GNP solution, DM1 (30 equivalents per GNP, 843 µg, 1.142 µmol, 843 µL; WuXi AppTec, Shanghai, China) in DMSO (Sigma-Aldrich) was added. The reaction was stirred at 800 rpm for 3 h at room temperature. After completion of the reaction, the solution was diluted to 10% (*v/v*) DMSO in H<sub>2</sub>O. Purification was performed using 10 kDa Amicon 15-Ultra filters. The final product was filtered with a 0.22 µm membrane and resuspended in H<sub>2</sub>O at a final target gold concentration of 5 mg/mL [18].

### 2.2.2. Peptide Functionalization of usGNPs

The coupling reagents Ethyl-3-(3-dimethylaminopropyl)carbodiimide (EDC, 3 equivalents per PEG(8)COOH, 8.5 mg, 44.162 µmol, 3.0 mL, Sigma-Aldrich) and N-Hydroxysuccinimide (NHS, six equivalents per PEG(8)COOH, 10.2 mg, 88.325 µmol, 3.0 mL, Sigma-Aldrich) in H<sub>2</sub>O were mixed and added to a GNP solution (40 mg Au, 2 mg/mL). The reaction was stirred at 600 rpm for 2 h at room temperature. A purification step was performed with 10 kDa Amicon 15-Ultra filters to remove the excess coupling reagents and the activated GNP was resuspended in 20 mL 1X phosphate buffered saline (PBS; Thermo Fisher Scientific, Waltham, MA, USA). cRGD-NH<sub>2</sub> or cRAD-NH<sub>2</sub> (WuXi AppTec) in 20 mL of 1X PBS were quickly added to the activated nanoparticles in two different amounts each (1.3–6.6 mg, 1.472–7.360 µmol) to obtain a high and a low loading (0.1 and 0.5 equivalents per PEG(8)COOH). The reaction was stirred at 600 rpm overnight at room temperature. Purifications were performed with 10 kDa Amicon 15-Ultra filters. The final products were filtered with a 0.22 µm membrane and resuspended in H<sub>2</sub>O at a final target gold concentration of 5 mg/mL [44].

### 2.2.3. Fluorophore Functionalization of GNPs

The coupling reagents Ethyl-3-(3-dimethylaminopropyl)carbodiimide (EDC, three equivalents per PEG(8)COOH, 2.5 mg, 13.249 µmol, 1.5 mL, Sigma-Aldrich) and N-hydroxysulfosuccinimide (Sulfo-NHS, six equivalents per PEG(8)COOH, 5.8 mg, 26.497 µmol, 1.5 mL, (Thermo Fisher Scientific) in H<sub>2</sub>O were mixed and added to a GNP solution (12 mg Au, 2 mg/mL). The reaction was stirred at 600 rpm for 2 h at room temperature. A purification step was performed with 10 kDa Amicon 15-Ultra filters to remove the excess of coupling reagents and the activated GNP was resuspended in 20 mL 1X PBS. Sulfo-Cyanine5 amine (Fluoroprobes, Scottsdale, AZ, USA) in 80 µL of DMSO was quickly added to the activated particle (0.05 equivalents per PEG(8)COOH, 0.16 mg, 0.221 µmol). The reaction was stirred at 600 rpm overnight at room temperature. Purifications were performed with 10 kDa Amicon 15-Ultra filters. The final products were filtered with a 0.22 µm membrane and resuspended in H<sub>2</sub>O at a final target gold concentration of 5 mg/mL.

## 2.3. Elemental Analysis; Microwave Plasma—Atomic Emission Spectrometry (MP-AES)

The gold concentration of the synthesized usGNPs in H<sub>2</sub>O was measured using 4200 MP-AES with MP Expert software version 1.5.16821 (Agilent, Santa Clara, CA, USA). Samples were digested with *Aqua regia*, then diluted using 3% (*v/v*) HCl.

## 2.4. Particle Sizing

### 2.4.1. UV-Vis Spectra

Spectra ( $\lambda$  350–700 nm) were obtained using Lambda 35 UV-Vis Spectrophotometer (PerkinElmer, Waltham, MA, USA) with a quartz cuvette (20 µg/mL Au, diluted in water).

### 2.4.2. Transmission Electron Microscopy (TEM)

Samples were prepared under ambient conditions by desiccating a 0.35 µL droplet of a 150 µg/mL Au GNP aqueous solution on a hydrophilized carbon film surface. Ul-

trathin film supports type #01824 (Ted Pella Inc., Redding, CA, USA) were used. The hydrophilization was performed for 2 min with 25 mA strong glow discharge treatment in a K100X plasma chamber (Quorum Technologies Ltd., Laughton, United Kingdom). Images were acquired in a transmission electron microscope of type JEM-2100F [Model EM-20014, UHR, 200 kV] (JEOL, Tokyo, Japan) equipped with a digital camera of type F-216 (TVIPS, Gauting, Germany). Wider field-of-view images at X150k magnification were assembled with the spotscan utility of the TVIPS EMMENU4 software from a beam shift based  $4 \times 4$  images matrix. Analyses were performed at CIC BiomaGUNE (San Sebastian, Spain). Data processing was performed using ImageJ (National Institutes of Health, Bethesda, MD, USA).

#### 2.4.3. Dynamic Light Scattering (DLS)

Size (hydrodynamic diameter) measurements were performed with Zetasizer Nano-ZS (Malvern Panalytical Ltd., Malvern, United Kingdom). Size was expressed by volume (%) as an average of three measurements taken at 25 °C at a 173-degree scattering angle in a plastic cuvette (200 µg/mL Au, diluted in 10X PBS).

#### 2.4.4. Differential Centrifugation Sedimentation (DCS)

Sizing analysis was performed using a CPS DC24000UHR disc centrifuge (CPS Instruments Inc., Prairieville, LA, USA) as described previously [18]. Eleven milliliters of 8–24% sucrose gradient was made up in water. Solutions with decreasing sucrose concentration were injected sequentially to create the gradient. Gradient evaporation was reduced by the injection of 500 µL dodecane. Prior to data acquisition, the gradient was allowed to reach thermal equilibrium and stabilize for about 30 min. A total of 0.237 µm polyvinylchloride (PVC) calibration standards in 50 µL injection volume were analyzed prior to each GNP sample (100 µL, 100 µg/mL Au) to ensure that the instrument was operating with a high degree of accuracy and optimally. Analyses were carried out at 24,000 rpm with the light detector adjusted to a position optimal for the analysis of usGNPs. Particle size was calculated based on an assumed GNP density of 5.0 g/cm<sup>3</sup>. Size was expressed by surface mode.

#### 2.5. Ligand Ratio; <sup>1</sup>H NMR

The GNP amount equivalent to 10 mg of Au was incubated with 600 µL of 0.3 M KCN in 0.1 M KOH (solvent D<sub>2</sub>O) after the removal of H<sub>2</sub>O by freeze-drying. Particles were incubated at 80 °C for 6 h with strong agitation to prevent pelleting (950 rpm). A transparent solution with no pellet indicated complete etching, which was visually checked. Experiments were performed at 298 K on a AVANCE III 500 spectrometer (Bruker, Billerica, MA, USA) at CIC BiomaGUNE (San Sebastian, Spain) (500 MHz, D<sub>2</sub>O). Data processing was performed using MestReNova 10.0.2 (Mestrelab Research S.L, A Coruña, Spain).

#### 2.6. UHPLC-CAD-MS

The GNP amount equivalent to 350 µg of Au was incubated with 15 µL of 0.3 M KCN and 0.01 M KOH and H<sub>2</sub>O up to 190 µL. Mixing was carried out by vortexing. Particles were incubated at 80 °C for 10 min with strong agitation to prevent pelleting (950 rpm). It was considered to have complete etching when, visually, a transparent solution with no pellet was attained. To the etched solution, 10 µL of 0.05 M TCEP that was made from a commercial, neutral 0.5 M solution (aqueous solution; pH 7.0 adjusted with ammonium hydroxide, Sigma-Aldrich) was added.

UltiMate 3000 Rapid Separation Liquid Chromatography system (Thermo Fisher Scientific) comprising a dual gradient standard pump, Corona Veo RS CAD detector (Chromeleon 7.0 software) in line with LCQ Fleet Ion trap Mass Spectrometer detector (Xcalibur 2.2 SP1 software) was used for all experiments. Separation steps were performed on an Acquity UPLC BEH C18 column, 130 Å, (100 × 2.1 mm i.d., 1.7 µm particle size) and an Acquity UPLC BEH C18 VanGuard precolumn, 130 Å, (5 × 2.1 mm i.d., 1.7 µm



particle size) (Waters, Milford, CT, USA). Solvents used as mobile phase were A: 0.1% formic acid in H<sub>2</sub>O; B: 0.1% formic acid in acetonitrile. Elution conditions: 0–0.5 min, 5% B isocratic; 0.5–6 min, linear gradient 5–98% B; 6–7 min, 98% B isocratic; washing and reconditioning of the column. The flow rate was 0.350 mL/min and the injection volume was 5 µL. The system operated at 35 °C. The Corona Veo RS Evaporation temperature was set at 35 °C; Power function: 1.0; Data collection Rate: 2 Hz; Signal Filter: 3.6 s. ESI-MS analysis was performed in the positive ion mode. Nitrogen was used as a desolvation gas. The ESI parameters of the source were: capillary temperature of 150 °C, the source heater temperature was held at 45 °C, and a potential of 3.8 kV was used on the capillary for positive ion mode. MS spectra, within the *m/z* range of 150–2000 amu, were obtained at 35 V cone voltage.

### 2.7. HPLC-MS

The GNP amount equivalent to 12 µg of Au was incubated with 60 µL of 0.5 M TCEP with 50% (*v/v*) DMSO/H<sub>2</sub>O up to 120 µL. Mixing was carried out by vortexing. Particles were incubated at 80 °C for 1 h with strong agitation to prevent pelleting (950 rpm). 1260 Infinity system (OpenLab CDS software) in line with 6120 Single Quadrupole mass spectrometer was used for all experiments (Agilent). Separations were performed on an Ascentis Express Peptide C-18 octadecyl phase column (4.6 × 100 mm, 2.7 µm) and an Ascentis Express C18 octadecyl phase guard column (4.6 × 5 mm, 2.7 µm (Sigma-Aldrich). Solvents used as mobile phase were A: 0.1% trifluoroacetic acid in H<sub>2</sub>O; B: 0.1% trifluoroacetic acid in acetonitrile for LC-DAD; A: 0.1% acetic acid in H<sub>2</sub>O; B: 0.1% acetic acid in acetonitrile for LC-MS. Elution conditions: 0–2 min, 20% B isocratic; 2–8 min, linear gradient 20–100% B; 8–9 min, 100% B isocratic; 9–10 min linear gradient 100–20% B; 10–12 min, 20% B isocratic; washing and reconditioning of the column.

The flow rate was 1 mL/min and the injection volume was 10 µL. The system operated at 35 °C. ESI-MS analysis was performed in the positive ion mode.

### 2.8. Octet Binding Studies

αVβ3 integrin was biotinylated by reacting 50 µL 1 mg/mL αVβ3 integrin (R&D systems, Minneapolis, MN, USA) with 5.2 µM EZ-Link NHS-PEG<sub>4</sub>-Biotin (Thermo Fisher Scientific) in PBS at room temperature for 1 h. The reaction was stopped by purification on a Zeba spin 7 kDa MWCO desalting column (Thermo Fisher Scientific) following the manufacturer's protocol [45].

Binding interactions were measured using an Octet Red 96 (Sartorius, Göttingen, Germany) with High Precision Streptavidin (SAX) biosensors as per the manufacturer's guidelines. In brief, biosensors were hydrated in binding buffer (50 mM HEPES, pH 7.4, 150 mM NaCl, 5 mM KCl, 0.1% (*w/v*) Bovine Serum Albumin (BSA; Sigma-Aldrich), 0.05% (*v/v*) Tween 20, 50 µM CaCl<sub>2</sub>) for >10 min, then washed twice in binding buffer (1 min then 3 min). Ten nanometers of biotinylated-αVβ3 integrin in binding buffer was loaded onto the biosensor for 15 min, quenched with 300 µM biocytin (Thermo Fisher Scientific) in binding buffer for 2 min, washed with binding buffer for 1 min, and the baseline in binding buffer measured for 3 min. αVβ3-loaded biosensors were allowed to associate with usGNPs in binding buffer for 40–60 min and dissociate in the buffer used for baseline measurements or in 1 µM cRGD-peptide in binding buffer for 40–60 min. To control for biosensor drift due to the dissociation of the αVβ3 monomers, measurements were referenced by subtracting the response from an αVβ3-loaded sensor with only a binding buffer in the association step. All measurements were taken at 30 °C.

The dissociation constant for the interaction was approximated by plotting the sensorgram response at equilibrium (averaged response at 3570–3600 s) against the nanoparticle concentration (assuming negligible depletion of the concentration of free usGNPs at equilibrium, [usGNP]<sub>free</sub> ≈ [usGNP]<sub>total</sub>). Results were normalized to give a percentage bound, to overcome any possible variation in R<sub>max</sub> (maximum response) due to the use of different batches of biotinylated-integrin and biosensors. Binding data were analyzed using Data

Analysis HT 10.0.1.7 (Sartorius). R was used to fit the equilibrium binding data to the Hill equation below using non-linear least square regression to estimate the dissociation constant ( $K_d$ ) and the Hill coefficient ( $h$ ).

$$\text{Fraction Bound} = \frac{[usGNP]^h}{K_d + [usGNP]^h} \quad (1)$$

### 2.9. Cell Lines and Routine Maintenance

U-87 MG [46], Hep3B, and HEK-293 cells were obtained from ATCC (Manassas, VA, USA). The U-251 MG cell line was a kind gift from Dr Cinzia Allegrucci at the University of Nottingham. The U-87 MG, Hep3B, and U-251 MG cells were routinely cultured and treated in EMEM (Sigma-Aldrich) supplemented with L-glutamine (Sigma-Aldrich), 10% (*v/v*) FBS (ATCC) non-essential amino acids (Sigma-Aldrich) and sodium pyruvate (Sigma-Aldrich). HEK-293 cells and their derivatives (see below) were maintained in low glucose DMEM (Thermo Fisher Scientific) supplemented with L-Glutamine, sodium pyruvate, and 10% (*v/v*) FBS (Thermo Fisher Scientific). Cells were kept at 37 °C, in a humidified atmosphere containing 5% CO<sub>2</sub>, unless stated otherwise.

### 2.10. Generation of $\alpha V\beta 3$ Integrin Expressing HEK-293 Cell Lines

HEK-293 cells were transfected with a plasmid harboring a Myc-DDK tagged CD61 ( $\beta 3$  integrin) cDNA (RC221606; OriGene, Rockville, MD, USA). The transfectants were selected with 500  $\mu\text{g}/\text{mL}$  G418 (Geneticin; Thermo Fisher Scientific). Surviving colonies were analyzed for expression with anti-FLAG immunofluorescence; the highest expressors with normal morphology were chosen for subsequent analysis. Generation and initial screening of clones were carried out by SAL Scientific Ltd. (Fordingbridge, UK).

### 2.11. Cellular Uptake of usGNPs

Cells were plated, at  $2 \times 10^6$  cells/well into collagen (10  $\mu\text{g}/\text{mL}$ ) coated 6-well plates (Eppendorf, Hamburg, Germany) and cultured overnight. The medium was exchanged for 400  $\mu\text{L}/\text{well}$  fresh low serum (2% [*v/v*] FBS) EMEM containing usGNPs at  $1 \times 10^8$  particles per cell (ppc) and incubated for 60 min as normal or at 4 °C. Competition experiments were preincubated with 500  $\mu\text{M}$  free cRGD-peptide in 300  $\mu\text{L}/\text{well}$  low serum EMEM for 60 min, then the usGNP solution was added at  $1 \times 10^8$  ppc in a 100  $\mu\text{L}$  volume (final volume 400  $\mu\text{L}/\text{well}$ ) and incubated for 60 min.

Post-treatment with usGNPs, the cells were scraped from the plates, transferred to 2 mL tubes, and centrifuged at  $200 \times g$  for 5 min. The supernatant was discarded, and the pellet was washed twice with 1 mL PBS, then once with 1 mL 0.2 M acetic acid (pH 2.8) in 0.5 M NaCl at 4 °C, to remove surface-bound material. Samples were centrifuged at  $200 \times g$  for 5 min and washed a further time with 1 mL PBS and stored at  $-20$  °C prior to analysis by ICP-MS.

Cell pellets were lysed in 1.6 mL 3% (*w/v*) tetramethylammonium hydroxide (TMAH; Sigma-Aldrich) solution containing 0.2% (*v/v*) Triton  $\times 100$  (Sigma-Aldrich) under agitation for approximately 30 min. A total of 1.55 mL of lysate was transferred into a new tube and topped up with 1 mL 3% (*w/v*) TMAH. Internal standard solution (2.45 mL of 4 ppb iridium (Sigma-Aldrich), 3% (*v/v*) HCl in H<sub>2</sub>O) was added to the samples and the resulting solution was measured on a NexION 300 $\times$  ICP-MS instrument (PerkinElmer) and quantitated using a calibration curve (Figure 4). Alternatively, usGNP uptake was measured using inductively coupled plasma—atomic emission spectroscopy (ICP-AES, Figure 5) using the iCAP 7400 ICP-AES Analyzer (Thermo Fisher Scientific) [47].

### 2.12. Cell Viability

Cells were plated at  $2 \times 10^4$  cells/well for Hep3B cells and  $1 \times 10^4$  cells/well for U-87 MG cells into 96-well plates (Eppendorf) and cultured overnight. The medium was exchanged for 200  $\mu\text{L}/\text{well}$  phenol red-free EMEM (Thermo Fisher Scientific) supplemented

with 10% (*v/v*) FBS, non-essential amino acids, and sodium pyruvate containing an 8-point 3-fold dilution series of compound or usGNP in triplicate. Cells were then incubated for 3-days as normal. Absorbance reading at 475 nm without pathlength correction was taken from all wells prior to the addition of XTT and PMS as follows. To each well of the plate 50  $\mu$ L 1 mg/mL 2,3-Bis-(2-Methoxy-4-Nitro-5-Sulfophenyl)-2H-Tetrazolium-5-Carboxanilide (XTT, Thermo Fisher Scientific) and 10  $\mu$ M phenazine methosulfate (PMS, Thermo Fisher Scientific) in phenol red-free EMEM was added. Cells were then incubated for 3 h as normal. Absorbance at 475 nm without pathlength correction was measured with SPECTROstar nano microplate reader (BMG Labtech, Ortenberg, Germany) and the corresponding  $A_{475\text{nm}}$  reading obtained before XTT/PMS incubation was subtracted. The subtracted data were normalized and an  $IC_{50}$  was obtained by fitting a four-parameter [Inhibitor] vs. response curve using Prism 9 (GraphPad Software, San Diego, CA, USA) [48].

### 2.13. Indirect Immunofluorescent Microscopy

Cells were seeded at  $1 \times 10^5$  in wells of a 24-well plate with glass coverslips, incubated overnight then treated as indicated. The medium was removed and the coverslips were rinsed with PBS twice. Cells were fixed on ice for 10 min with 4% paraformaldehyde in 250 mM HEPES pH 7.4 (both from Sigma-Aldrich). For detecting intracellular antigens cells were permeabilized with 0.1% Triton X-100 (Thermo Fisher Scientific) in PBS for 20 min on ice. Coverslips were then incubated for 1 h at 37 °C in a blocking buffer (10% FBS, 0.1% Triton X-100 in PBS). Coverslips were then placed in a humidity chamber and incubated overnight at 4 °C with 15  $\mu$ L of primary antibody solution in blocking buffer diluted as follows: mouse anti-human integrin  $\beta 3$  primary antibody, 1:200 (11–0519-42; Thermo Fisher Scientific); rabbit anti-EEA1, 1:200 (3288; Cell Signaling Technology, Danvers, MA, USA); rabbit anti-RAB7, 1:100 (9367; Cell Signaling Technology); rabbit anti-RAB11, 1:100 (5589; Cell Signaling Technology); rabbit anti-RCAS1, 1:100 (12290; Cell Signaling Technology). Coverslips were washed 4 $\times$  for 10 min with PBS with gentle rocking, then were subsequently incubated with 100  $\mu$ L of Alexa Fluor 488 conjugated goat anti-mouse secondary antibody (1:800 dilution, A11001; Thermo Fisher Scientific) or Alexa Fluor 488 conjugated goat anti-rabbit secondary antibody (1:800 dilution, A11008; Thermo Fisher Scientific) at 37 °C for 1 hr. The coverslips were washed 4 $\times$  with PBS as above, then with ultrapure water, dried, and mounted onto microscope slides using Vectashield<sup>®</sup> mounting medium containing DAPI (Vector Laboratories Inc., Newark, NJ, USA). Imaging was performed on a TCS SP8 laser scanning microscope with an HC PL APO 63 $\times$ /1.40 Oil CS2 objective (Leica Microsystems, Wetzlar, Germany). Image acquisition and processing parameters were kept identical between samples from the same experiment to ensure comparability.

### 2.14. Flow Cytometry

Cells were seeded at  $1 \times 10^4$  per well in a 6-well plate and incubated for 24 h. Cells were detached using 0.5% trypsin (Thermo Fisher Scientific), suspended in 2 mL of PBS then collected in a conical centrifuge tube. Samples were centrifuged at 220 $\times$  g for 3 min, then suspended in 1 mL PBS + 0.3% BSA (Sigma-Aldrich). All samples were filtered using a 100  $\mu$ m Corning cell strainer (Thermo Fisher Scientific). Cells were counted using TC20<sup>™</sup> Automated Cell Counter (Bio-Rad Laboratories, Hercules, CA, USA). Cell density was set to  $1 \times 10^6$ , and 25  $\mu$ L of cell suspension was then incubated with 25  $\mu$ L FITC pre-conjugated primary antibodies (mouse anti-human integrin  $\beta 3$ ; 11–0519-42, 1:200; Thermo Fisher Scientific) or isotype control antibodies (mouse IgG kappa isotype control; 11–4714-42, 1:200; Thermo Fisher Scientific) for 30 min at room temperature in U bottom 96 well plates. Samples were centrifuged at 260 $\times$  g for 2 min. Cells were then washed three times in 100  $\mu$ L PBS + 0.3% BSA, then resuspended in 200  $\mu$ L PBS + 0.3% BSA. The samples were transferred into a FACS tube with 200  $\mu$ L FACS sheath fluid. Cells were analyzed by flow cytometry using a FACSVerse flow cytometer (Becton, Dickinson and Company, Franklin Lakes, NJ, USA). A minimum of 10,000 cells were analyzed per sample. Data were

collected and analyzed using FACSuite and FlowJo software packages (Becton, Dickinson and Company).

### 2.15. Live Cell Imaging

Cells were seeded in 35 mm  $\mu$ -dish (ibidi) or Nunc Lab-Tek II 8-well coverglass (Thermo Fisher Scientific) vessels at  $2.85 \times 10^4$  cells per  $\text{cm}^2$ , incubated overnight then treated as indicated in the figure legends with chlorpromazine-hydrochloride (Sigma-Aldrich), genistein (Sigma-Aldrich), or nocodazole (Sigma-Aldrich). Live cell imaging was performed on a TCS SP8 laser scanning confocal microscope with an HC PL APO 63 $\times$ /1.40 Oil CS2 objective. Cells were stained as indicated in the figure legends with BOD-IPY™ FL C5-Lactosylceramide BSA complex (Thermo Fisher Scientific) or LysoTracker® Red (Thermo Fisher Scientific). Multiple dyes were imaged with sequential acquisition settings to ensure a clear signal from single dyes without bleed-through into other acquisition channels.

## 3. Results and Discussion

### 3.1. Synthesis and Characterization of Functionalized Gold Nanoparticles

In order to characterize the uptake of ultras-small gold nanoparticles functionalized with cRGD and to prove that they can deliver cytotoxic cargo to cells, plasmonic GNPs with 4 nm cores were synthesized using a modified aqueous Brust-Schiffrin method [49–51]. Two types of ligands were used in a 50:50 ratio to make base usGNPs: a monosaccharide with a short ethyl side chain 2'-Thioethyl  $\alpha$ -D-galactopyranoside ( $\alpha$ -Galactose-C<sub>2</sub>) and an oligoethylene glycol  $\alpha$ -Thio- $\omega$ -(propionic acid) octa(ethylene glycol) (PEG(8)COOH). Two-nanometer core GNPs functionalized with the same mixed corona and the SIKVAV peptide have been previously demonstrated to have the ability to target cancer cells through  $\alpha$ 6 $\beta$ 1 integrins [52]. A similar structure with a 2 nm core functionalized with cRGD and the same negatively charged oligoethylene glycol ligand also showed promising results in vitro [53]. Carbohydrates are known for their ability to improve stability (avoid aggregation), solubility, biocompatibility, biodegradability and confer stealth (protein-repellent) properties [54]. Polyethylene glycols (PEG), among them oligoethylene, are flexible molecules, relatively inert (non-immunogenic), and soluble in water, as well as most polar organic solvents. They possess a strong ability to stabilize particles by preventing nanoparticle aggregation [55,56]. They also improve the characteristics of the nanoparticles in vitro and in vivo, such as half-life or oral bioavailability [57]. The terminal functional group of PEG can additionally be used to bind to molecules presenting a complementary moiety to achieve active targeting [2]. According to the model of Vergara et al. [58], the 4 nm GNPs are composed of an average of 2000 gold atoms and 290 ligands and henceforth depicted as (Ligands)<sub>290</sub>@Au<sub>2000</sub>. The base particle obtained through the modified Brust-Schiffrin synthesis: ( $\alpha$ -Galactose-C<sub>2</sub>)<sub>145</sub>(PEG(8)COOH)<sub>145</sub>@Au<sub>2000</sub> was then functionalized using two strategies: post-functionalization and ligand exchange. Post-functionalization was performed by amidation of the carboxyl-terminal moiety of the oligoethylene glycol ligand with amine derivatives of cRGD, cRAD (similar structure but with lower affinity to  $\alpha$ V $\beta$ 3 integrin) [59,60], and the Sulfo-Cyanine5 amine fluorophore [61,62]. Ligand exchange strategy was used to load DM1 [18,63] (Figure 1).



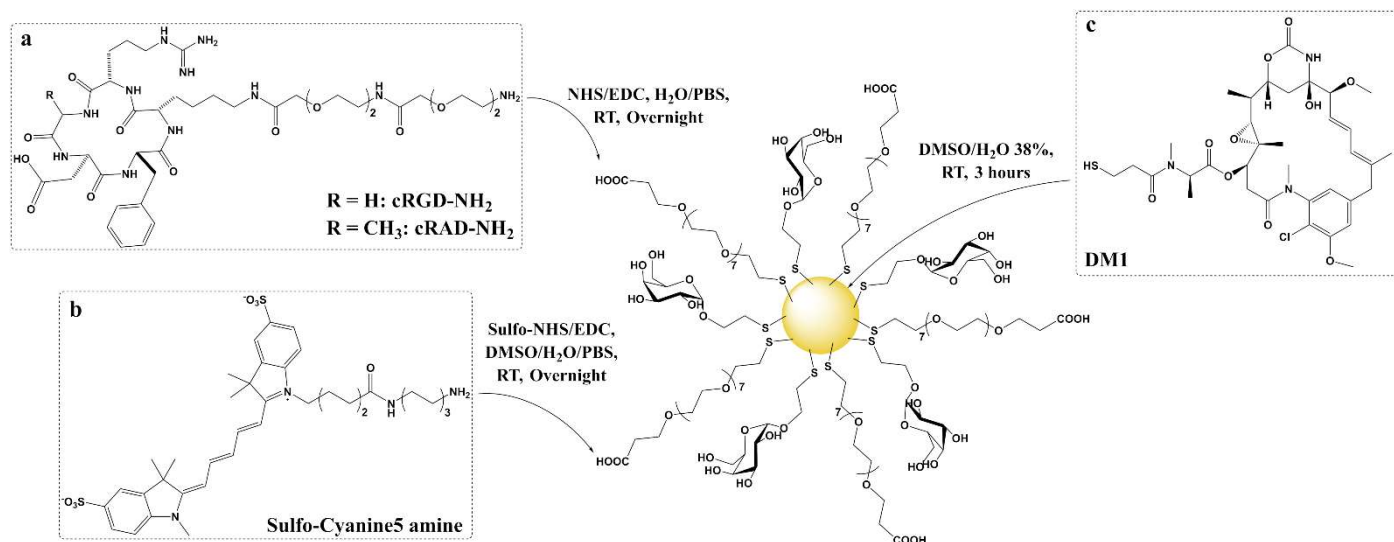


**Figure 1.** Four nanometers core usGNP platform ( $\alpha$ -Galactose-C<sub>2</sub>)<sub>145</sub>(PEG(8)COOH)<sub>145</sub>@Au<sub>2000</sub> composed of 2'-Thioethyl  $\alpha$ -D-galactopyranoside and  $\alpha$ -Thio- $\omega$ -(propionic acid) octa(ethylene glycol) synthesized with a modified Brust-Schiffrin method. (a) cRGD and cRAD amine derivatives and (b) Sulfo-Cyanine5 amine fluorophore moieties are bound through post-functionalization (amide coupling). (c) DM1 is linked by ligand exchange (direct anchoring to the core through a thiol group).

The post-functionalization synthetic procedure permitted the control of the number of cRGD moieties loaded per usGNP using simple stoichiometric variations of a cRGD amine derivative (cRGD-NH<sub>2</sub>). Consequently, two different versions were synthesized: High cRGD-usGNP and Low cRGD-usGNP with approximately 60 and 20 cRGD units per usGNP, respectively. The same method was applied to obtain High cRAD-usGNP and Low cRAD-usGNP. The base usGNPs and Low cRGD-usGNPs were functionalized with approximately 20 DM1 per GNP. 1–2 Sulfo-Cyanine5 amine was added to the usGNPs for fluorescent studies (Cy5-usGNP) (Table 1).

**Table 1.** Chemical formula of the different usGNPs determined by <sup>1</sup>H NMR and LC methods depicted using the (Ligands)<sub>290</sub>@Au<sub>2000</sub> model [58], hydrodynamic diameter (volume distribution) as established by DLS and diameter by DCS (surface mode). N.D.: not determined.

usGNP	(Ligands) <sub>290</sub> @Au <sub>2000</sub> Model	Hydrodynamic Diameter by DLS (mean; nm)	Diameter by DCS (mean; nm)
Base usGNP	( $\alpha$ -Galactose-C <sub>2</sub> ) <sub>145</sub> (PEG(8)COOH) <sub>145</sub> @Au <sub>2000</sub>	9.1	9.7
High cRGD-usGNP	( $\alpha$ -Galactose-C <sub>2</sub> ) <sub>145</sub> (PEG(8)COOH) <sub>85</sub> (cRGD) <sub>60</sub> @Au <sub>2000</sub>	11.4	10.1
Low cRGD-usGNP	( $\alpha$ -Galactose-C <sub>2</sub> ) <sub>145</sub> (PEG(8)COOH) <sub>125</sub> (cRGD) <sub>20</sub> @Au <sub>2000</sub>	10.2	9.6
High cRAD-usGNP	( $\alpha$ -Galactose-C <sub>2</sub> ) <sub>145</sub> (PEG(8)COOH) <sub>85</sub> (cRAD) <sub>60</sub> @Au <sub>2000</sub>	12.4	10.0
Low cRAD-usGNP	( $\alpha$ -Galactose-C <sub>2</sub> ) <sub>145</sub> (PEG(8)COOH) <sub>125</sub> (cRAD) <sub>20</sub> @Au <sub>2000</sub>	11.5	9.9
DM1-cRGD-usGNP	( $\alpha$ -Galactose-C <sub>2</sub> ) <sub>135</sub> (PEG(8)COOH) <sub>115</sub> (cRGD) <sub>20</sub> (DM1) <sub>20</sub> @Au <sub>2000</sub>	N.D.	N.D.
DM1-usGNP	( $\alpha$ -Galactose-C <sub>2</sub> ) <sub>135</sub> (PEG(8)COOH) <sub>135</sub> (DM1) <sub>20</sub> @Au <sub>2000</sub>	N.D.	N.D.

Different analytical techniques were employed to characterize the core and overall size of the usGNPs. UV-Vis spectroscopy displayed a surface plasmon band (SPR) with a local maximum of around 520 nm (Figure 2a). Transmission Electron Microscopy (TEM) showed a mean core size of 4 nm (Figure 2b). Dynamic Light Scattering (DLS, Figure 2c, Table 1) and Differential Centrifugation Sedimentation (DCS, Figure 2d) confirmed the monodispersity and that despite functionalizations, the particles remain in the ultrasmall (<10 nm) range (Table 1).

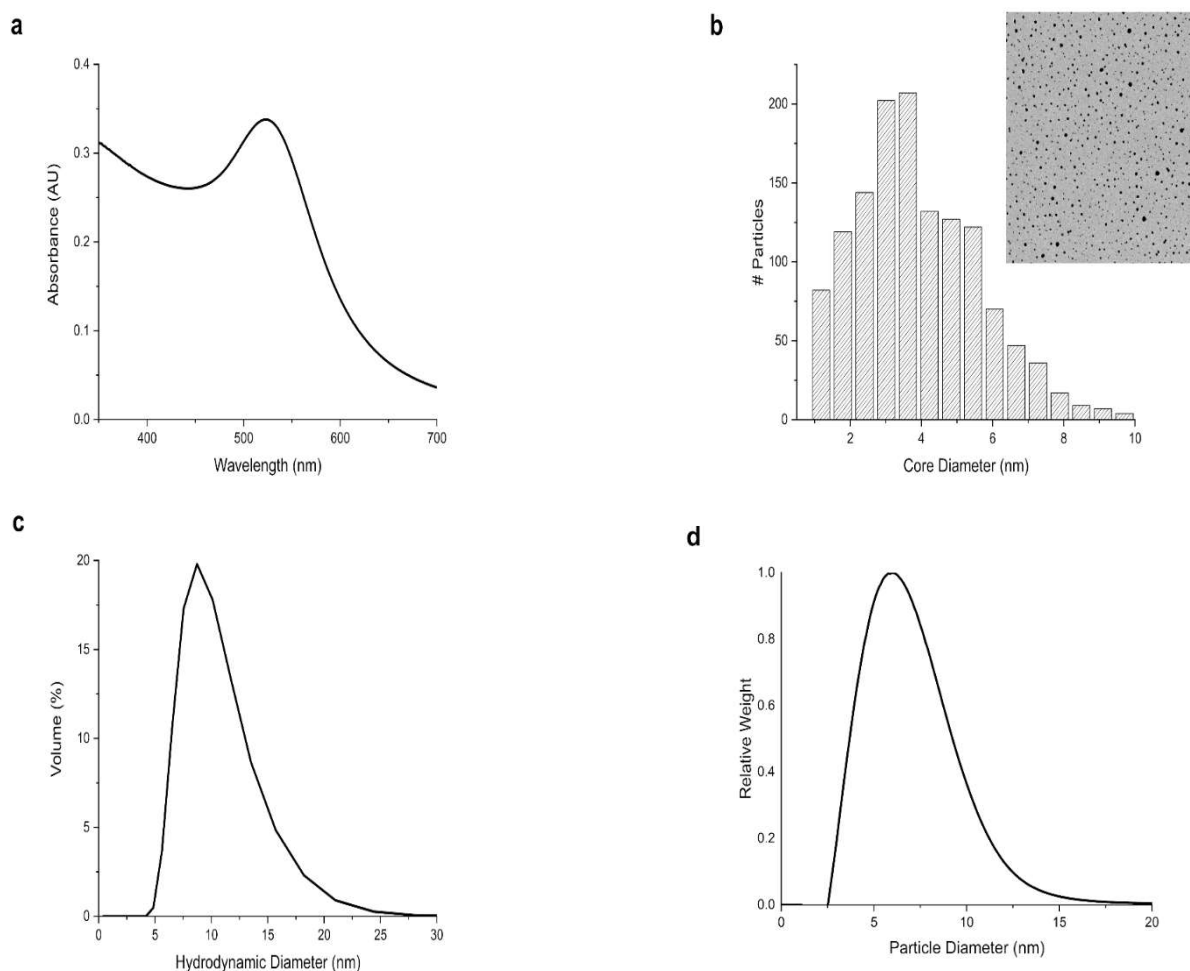


**Figure 2.** Characterization of the size and dispersity of usGNPs. (a) UV-Vis spectrum ( $\lambda$  350–700 nm) shows a surface plasmon band with a local maximum at  $\sim$ 520 nm. (b) TEM picture and core size distribution indicate a mean core size of 4 nm. (c) DLS hydrodynamic size distribution by volume and (d) DCS diameter distribution confirm monodispersity and that functionalized particles remain in the ultrasmall range.

Proton Nuclear Magnetic Resonance ( $^1\text{H}$  NMR, Figure S1 in the Supplementary Materials) and Liquid Chromatography (LC) with different detectors (UV, Charged Aerosol Detector (CAD) or Mass Spectrometer (MS)) were used to characterize the ligand corona.  $^1\text{H}$  NMR and LC analyses were performed after core etching and ligand release using a solution of potassium cyanide in potassium hydroxide (KCN/KOH) [64,65]. For LC applications, tris(2-carboxyethyl)phosphine (TCEP), a disulfide bond reducer, was added to prevent spontaneous thiol oxidation of the ligands after release from the core. A single method of LC-CAD-MS was used to determine the relative amounts of the base GNP ligands, cRGD, cRAD, and the fluorophore (Figure S2) by dividing the area of the peaks obtained with the CAD detector by the molecular weight of each ligand [66,67]. Absolute DM1 quantification was performed separately by LC-MS ( $\lambda$  276 nm, Figure S3). The relative amounts (or absolute for DM1) of the ligands obtained by  $^1\text{H}$  NMR and LC analyses were then fitted in the previously mentioned model of Vergara et al. [58] with a total amount of 290 ligands per GNP (Table 1). The 1:1 ratio between  $\alpha$ -Galactose- $\text{C}_2$  and PEG(8)COOH in the corona of the Base usGNP was measured by both  $^1\text{H}$  NMR and LC-CAD. Equally, both techniques validated the high (60 per GNP) and low (20 per GNP) loading of the peptides. Sulfo-Cyanine5 amine loading was only measured by LC-CAD (1–2 Fluorophores per GNP). DM1 quantification in mg/mL was converted into equivalents per GNP (20 DM1 per

GNP). The results presented above suggest a significant improvement on our previous GNP design based on a 2 nm core that can carry eight SIKVAV ligands per 200 gold atoms [52]. The slightly increased size still puts the 4 nm design in the ultrasmall range keeping its advantages outlined above, but it can support at least a 6x increase in cargo-bearing capacity.

### 3.2. Functionalized usGNPs Bind $\alpha V\beta 3$ Integrin

$\alpha V\beta 3$  integrin binding and release of cRGD functionalized usGNPs were measured with biolayer interferometry [45]. First,  $\text{HighcRGD-usGNP}$  and control base usGNP were used to assess the specificity of binding to the immobilized  $\alpha V\beta 3$  integrin.  $\text{HighcRGD-usGNP}$  showed robust binding with a  $K_d$  of  $29.2 \pm 3.2$  pM ( $p < 0.01$ ) and a Hill coefficient (h) of  $1.11 \pm 0.25$  ( $p < 0.05$ ). In the absence of cRGD, the binding of 1 nM control base usGNP to the immobilized  $\alpha V\beta 3$  integrin was unmeasurable, suggesting the absence of non-specific binding to  $\alpha V\beta 3$  integrin of any of the components of the base particle (Figure 3a). The very low  $K_d$  measured for  $\text{HighcRGD-usGNP}$  suggests that avidity due to a large number of cRGD moieties may play a role in the binding, with little or no cooperativity (h is approximately 1). As expected, the  $\text{LowcRGD-usGNP}$  had a weaker affinity dropping approximately 100-fold (Figure 3b) with a  $K_d$  of  $3.2 \pm 0.4$  nM ( $p < 0.001$ ) and h of  $0.44 \pm 0.03$  ( $p < 0.001$ ). The negative cooperative binding highlighted by the Hill coefficient  $< 1$  is likely due to electrostatic repulsion between nanoparticles densely bound to the sensor, which becomes apparent at high usGNP concentrations. Importantly, the data on  $\text{LowcRGD-usGNPs}$  suggest that high-affinity binding (3.2 nM) is still possible with the lower cRGD loading, therefore leaving room for the conjugation of a drug payload.

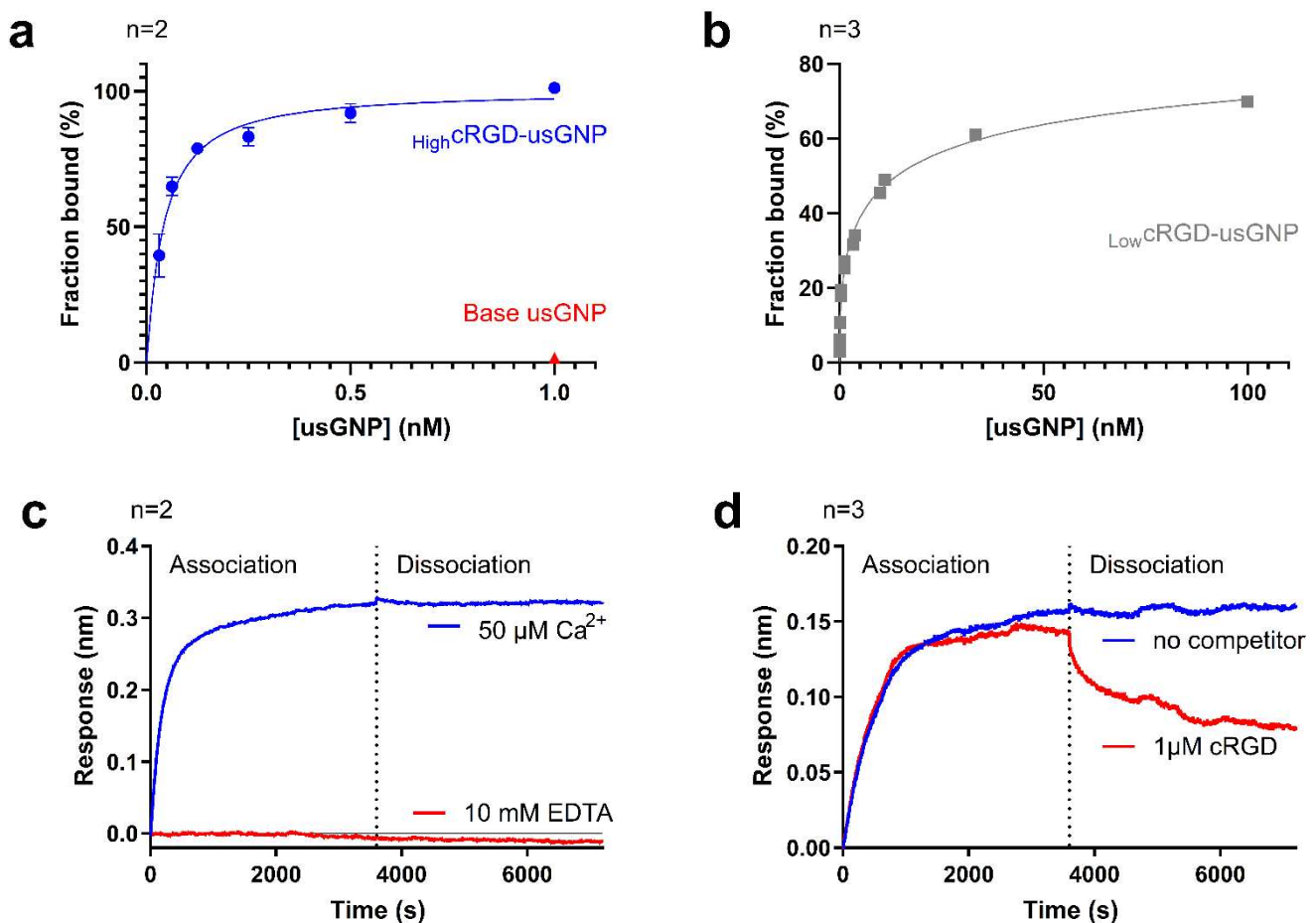


**Figure 3.** cRGD conjugated to usGNPs retain binding affinity to  $\alpha V\beta 3$  integrin. (a) Binding of  $\text{HighcRGD-usGNP}$  to immobilized  $\alpha V\beta 3$  integrin.  $K_d = 29.2 \pm 3.2$  pM ( $p < 0.01$ ;  $R^2 = 0.991$ ). No binding of the base usGNP was seen at the top concentration. (b) Binding of  $\text{LowcRGD-usGNP}$  to immobilized

$\alpha V\beta 3$  integrin. cRGD density significantly alters binding affinity.  $K_d = 3.2 \pm 0.4$  nM ( $p < 0.001$ ;  $R^2 = 0.995$ ). Error bars represent standard deviation (SD) of  $n$  independent repeats (a,b). (c) Binding of cRGD-usGNPs is  $Ca^{2+}$ -dependent: 0.25 nM  $_{High}$ cRGD-usGNP was bound onto a biosensor with immobilized  $\alpha V\beta 3$  integrin in the presence of 50  $\mu M$   $Ca^{2+}$ . Note the absence of binding and increased instability of the immobilized  $\alpha V\beta 3$  integrin dimer in the presence of 10 mM EDTA. (d) Binding onto the biosensor is cRGD-mediated: 0.25 nM cRGD-usGNP bound to immobilized  $\alpha V\beta 3$  integrin dissociates when 1  $\mu M$  free cRGD is added as a competitor to the dissociation buffer. (c,d) Representative figures of  $n$  independent repeats.

The binding of the cRGD-usGNP to immobilized  $\alpha V\beta 3$  integrin was  $Ca^{2+}$  dependent as evidenced by the absence of binding in the presence of 10 mM EDTA (Figure 3c), which is a long-known property of the interaction between cRGD-peptide and  $\alpha V\beta 3$  integrin [68]. Figure 3c also shows that the dissociation of cRGD-functionalized usGNPs from the immobilized  $\alpha V\beta 3$  integrin was undetectable over 1 h. The addition of 1  $\mu M$  cRGD-peptide to the dissociation buffer resulted in a reduction in response during the dissociation phase (Figure 3d), suggesting that the addition of the peptide is causing competitor-induced dissociation of the cRGD-usGNP from the immobilized integrin [69]. The slow dissociation rate of the cRGD-usGNP could be either due to an avidity effect from the multiple cRGD-ligands decorating the usGNP, and/or the high density of the gold-core reducing the rate of diffusion of the usGNP making rapid rebinding of the usGNP to the integrin more likely [69].

### 3.3. Functionalized usGNPs Are Taken up by Cells by an $\alpha V\beta 3$ Integrin Mediated Mechanism

To test the uptake of cRGD functionalized usGNPs, pairs of cell lines with high and no or very low  $\alpha V\beta 3$  integrin expression but otherwise similar characteristics were chosen. The U-87 MG glioblastoma cell line [46] has been reported to highly express  $\alpha V\beta 3$  integrin [70–74], while the U-251 MG [71,73] is a limited  $\alpha V\beta 3$  expressor. While both these cell lines are of glioblastoma origin, they are genetically different, for which ectopic expression of the  $\alpha V\beta 3$  integrin was established in the HEK-293 human embryonic kidney cell line that does not normally express this receptor. Expression was confirmed by flow cytometry and immunofluorescent microscopy (Figure S4). The uptake of usGNPs was characterized and quantitated with elemental analysis of the gold content by inductively coupled plasma mass spectrometry (ICP-MS) and confocal microscopy using a set of usGNPs functionalized with Sulfo-Cyanine5 amine.

Using the U-87 MG cell line, which expresses a high level of  $\alpha V\beta 3$  integrin, the uptake of usGNPs with different characteristics was quantified with ICP-MS and visualized with live cell confocal microscopy. While the uptake of the base usGNPs was minimal, a substantial amount of  $_{Low}$ cRGD-usGNPs was taken up by the cells, which increased by  $\sim 3.4$ -fold from  $\sim 4.9 \times 10^6$  to  $\sim 16.7 \times 10^6$  usGNPs per cell by an increased density of cRGD peptides on the surface of the  $_{High}$ cRGD-usGNPs (Figures 4a and 5a–c). usGNPs, functionalized with cRAD peptide that has a low affinity to the  $\alpha V\beta 3$  integrin [75,76], showed a comparatively low uptake ( $\sim 1.6 \times 10^6$  and  $\sim 2.7 \times 10^6$  for  $_{Low}$ cRAD and  $_{High}$ cRAD-usGNPs, respectively; Figure 4a). Pre-incubating the cells with 500  $\mu M$  cRGD-peptide resulted in a reduction in usGNP uptake to a level ( $\sim 2 \times 10^5$  usGNPs per cell) similar to that found for the base usGNP ( $\sim 10^5$  usGNPs per cell) confirming the target specificity (Figure 4b). Reducing the temperature to 4  $^\circ C$  resulted in a 7-fold loss in uptake from  $\sim 2.7 \times 10^6$  to  $\sim 3.8 \times 10^5$  usGNPs per cell (Figure 4c), confirming that uptake is via an active process.



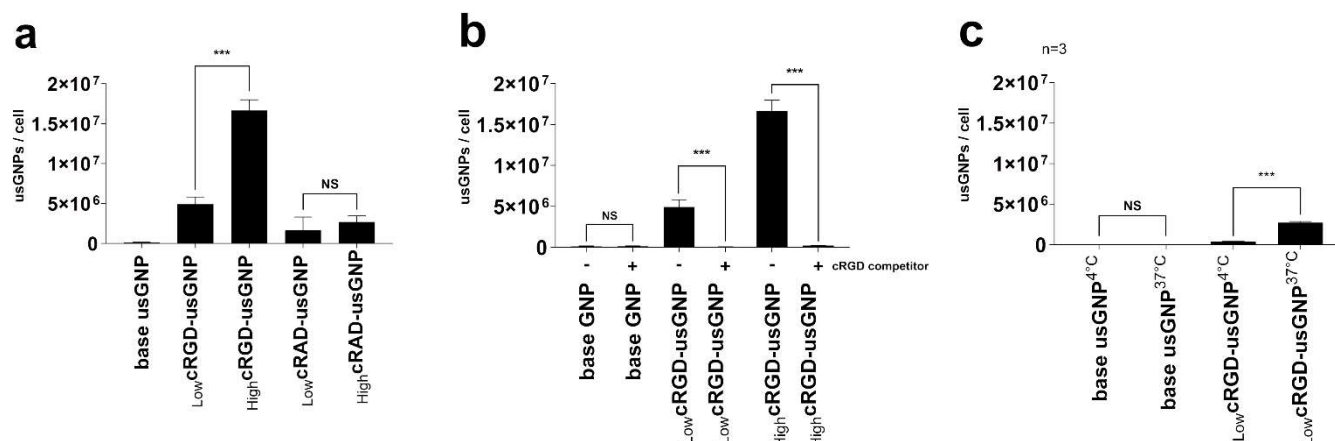


**Figure 4.** Uptake of usGNPs by U-87 MG cells is mediated via interaction with cRGD sidechains. Cells were incubated with the indicated usGNPs for 60 min then internalized gold was quantified with ICP-MS. (a) Uptake efficiency is dependent on the number of cRGD molecules loaded on the usGNPs. The cRAD low-binding peptide mediates only limited uptake by these cells. (b) Pre-treatment of cells with free cRGD peptides (+) interferes with the uptake of usGNPs, which confirms that uptake is  $\alpha V\beta 3$  integrin-mediated. (c) Uptake of usGNPs is an active process as incubating the cells with the cRGD-usGNPs at 4 °C results in the reduction of uptake. Error bars represent SD of n independent repeats. NS:  $p > 0.05$ ; \*\*\*:  $p \leq 0.001$ .

The dependency of uptake on  $\alpha V\beta 3$  integrin expression by host cells was established using the verified cell line pairs and experiments using confocal microscopy and gold content by inductively coupled plasma atomic emission spectroscopy (ICP-AES). As expected, the uptake of cRGD-loaded usGNPs by the U-87 MG cell line was visible after 1 h, while no uptake was seen by the U-251 MG cell line (Figure 5c,d). Surprisingly, no uptake was seen by HEK-293 clone 5, a sufficiently high  $\alpha V\beta 3$  integrin expression which was confirmed earlier (Figure S4). ICP-AES confirmed uptake by U-87 MG cells. Furthermore, with this technique limited uptake by U-251 MG cells was also visible, in line with their limited albeit not zero  $\alpha V\beta 3$  integrin expression (Figure 5e). However, uptake by the parental HEK-293 or its  $\alpha V\beta 3$  integrin expressing derivative clone 5, could not be shown. Treatment of clone 5 cells with  $\text{High cRGD-usGNPs}$  induced their detachment from the substrate making detection and measurement of uptake unreliable (data not shown). HEK-293 cells express the  $\alpha V$  integrin subunit, which forms the RGD binding integrin heterodimers pairing with a  $\beta$  subunit [10]. Of these, HEK-293 cells express  $\beta 1$ , but not  $\beta 3$ ,  $\beta 5$  or  $\beta 6$  [77]. RGD binding integrins tend to have distinct subcellular localization patterns [78], which could be imbalanced by the ectopic expression of  $\beta 3$  together with the assembly and function of clathrin-coated structures. Furthermore, ectopic expression of the  $\beta 3$  subunit has also been reported to transform apoptotic signaling pathways characteristic to endothelial cells into epithelial HEK-293 cells [79]. These imbalances could explain the detachment of our  $\text{High cRGD-usGNP}$  treated clone 5 cells, nevertheless, we observed no unusual cell death of the untreated CD61-HEK-293 cells.

These data strongly indicate that the uptake of usGNPs is cRGD-dependent, possibly through an endocytic mechanism mediated by binding to the  $\alpha V\beta 3$  integrin.

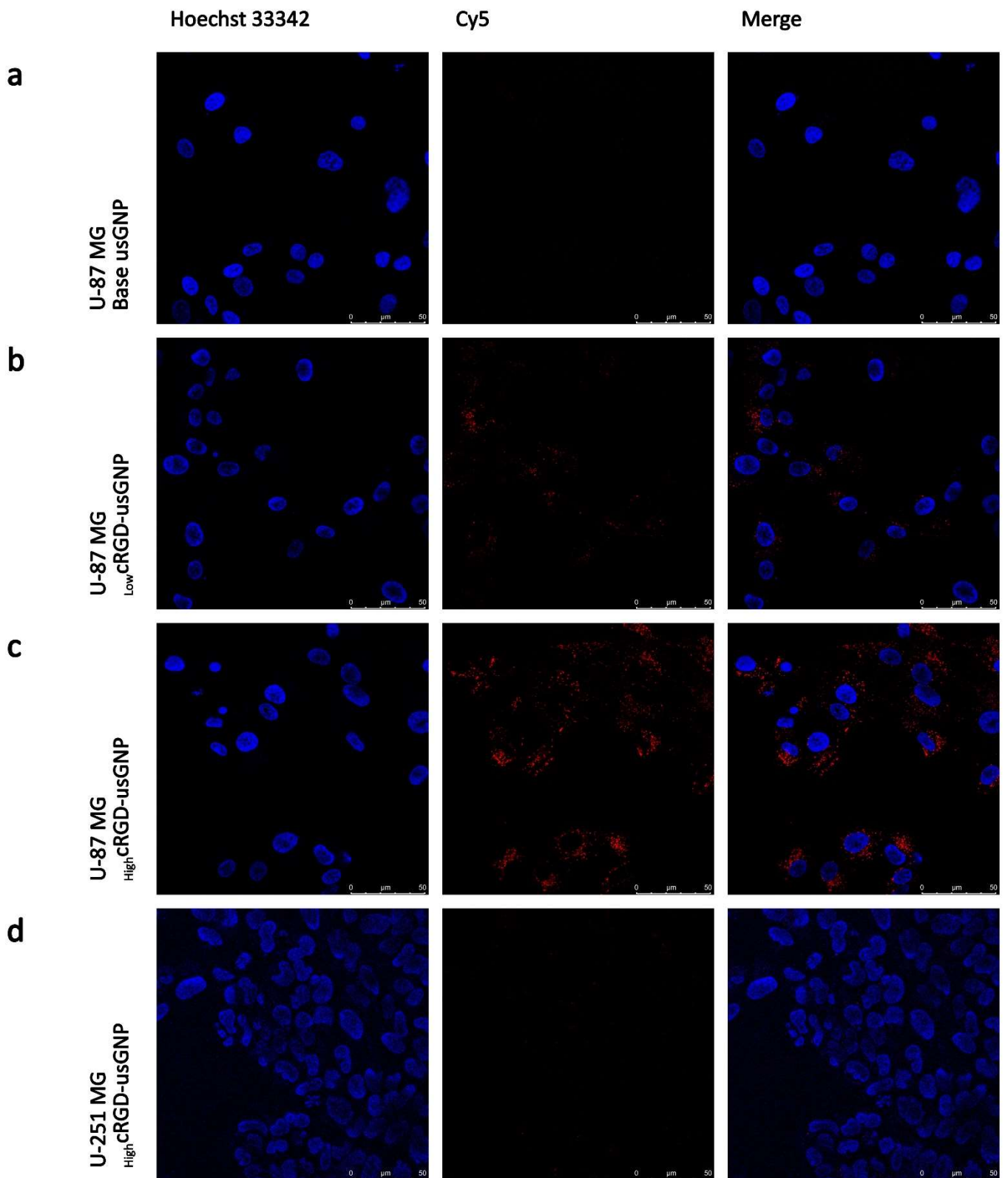
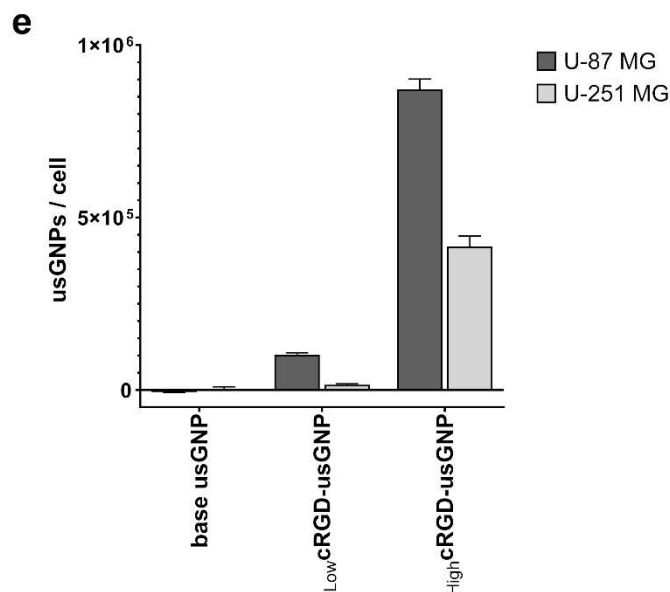


Figure 5. Cont.



**Figure 5.** Uptake of usGNPs depends on  $\alpha V\beta 3$  integrin expression level. (a–d) U-87 MG and U-251 MG cells were incubated with 9 nM usGNPs with indicated cRGD densities for 2 h, then stained with 1  $\mu\text{g}/\text{mL}$  Hoechst 33342 and imaged with live cell confocal microscopy. (e) Internalized usGNP content was quantified with ICP-AES following 2 h incubation. Representative figure from three (U87-MG) and one (U251-MG) independent repeats; error bars represent SD of five technical replicates.

### 3.4. usGNP Uptake Is Mediated through Clathrin-Dependent Mechanisms

Integrin-mediated endocytosis occurs via several distinct pathways [10]. In order to gain insight into which of these is utilized for the uptake of functionalized usGNPs, specific inhibitors of clathrin-dependent and -independent mechanisms were employed (Figure S5). We observed significant cytotoxicity using chlorpromazine-hydrochloride (CPH) at concentrations other laboratories employed. At the lowest concentration (2.5  $\mu\text{g}/\text{mL}$ ) distribution of endocytosed BODIPY<sup>TM</sup> FL C5-Lactosylceramide BSA complex (LaCer), which is endocytosed via the clathrin-independent route [80], was normal without signs of cytotoxicity; however, at higher concentrations membrane blebbing was observed, and the cytoplasm was filled with the signal from LaCer indicating compromised membrane integrity (Figure S6). Consequently, for subsequent experiments, 2.5  $\mu\text{g}/\text{mL}$  CPH was used to inhibit clathrin-dependent endocytosis. Cytotoxicity of genistein, an inhibitor of clathrin-independent endocytosis was also tested, but no such effect was found in the applied concentration range (data not shown). Challenges of selective pharmacological inhibition of uptake mechanisms due to toxicity have also been highlighted by other laboratories [81].

To assess which endocytic pathway was responsible for the internalization of usGNPs, U-87 MG cells were pre-treated with CPH, genistein, and nocodazole, a microtubule poison, and inhibitor of intracellular trafficking [82], or left untreated, then incubated with High cRGD-usGNPs and LaCer together for 2 h. Uptake of High cRGD-usGNPs was inhibited by CPH but not by genistein, while uptake of the LaCer control was inhibited by genistein and not by CPH (Figure 6a–d). Nocodazole treatment moderately interfered with the internalization and intracellular trafficking of both High cRGD-usGNPs and LaCer (Figure 6e), similar to the reported, cell type-specific, effect found by other laboratories [82]. These results indicate that the High cRGD-usGNPs are internalized via the clathrin-dependent endocytic pathway. cRGDfK functionalized 50 nm GNPs have been reported to similarly internalize via clathrin-dependent routes, although sensitivity of uptake to the macropinocytosis inhibitor 5-(N-ethyl-N-isopropyl) amiloride (EIPA) was also found [70]. An uptake of non-targeted nanoparticles has been reported to be cell-type specific [81] and was also found to be dependent on surface properties [83], which highlights the importance of

functionalization to target nanoparticles to specific receptors, such as cRGD targeting to  $\alpha V\beta 3$  integrin in our design.

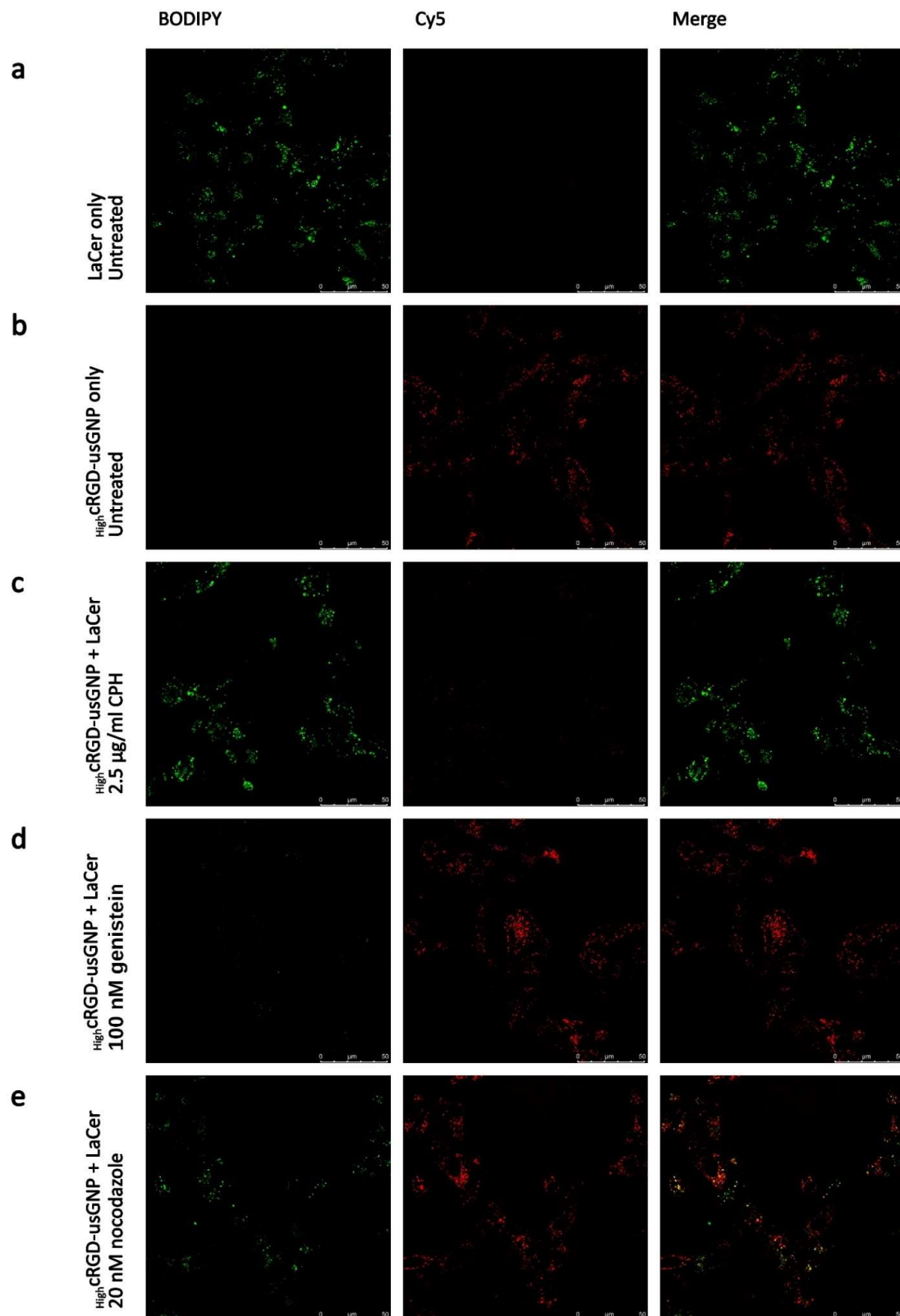


**Figure 6.** Inhibition of uptake of  ${}^{\text{High}}$ cRGD-usGNPs and LaCer control in U-87 MG cells. (a–e) Cells were pre-treated with the indicated drugs for 30 min, then  ${}^{\text{High}}$ cRGD-usGNPs at 9 nM final concentration



and 1 µg/mL LaCer were added. Live cell images were acquired following a 2 h incubation, with filter settings optimized for BODIPY (LaCer, pseudo-colored green) and Cy5 (HighcRGD-usGNPs, red).

### 3.5. Internalized usGNPs Accumulate in the Lysosomes

The moderate sensitivity of internalization to nocodazole prompted further analysis of intracellular trafficking of our functionalized usGNPs. Uptake and localization of Cy5 labeled HighcRGD-usGNP were followed in live cell imaging in U-87 MG cells labeled with LysoTracker® Red 15 min before microscopy. The presence of usGNPs in lysosomes, indicated by co-localization of the LysoTracker® Red and Cy5 signals, became obvious after 30 min of incubation and reached a maximum after 120 min (Figure 7). Similar uptake kinetics of 4nm fluorescein-PEG-tagged usGNPs was observed in Raw264.7 macrophage cells with limited usGNP accumulation after 15 min that gradually increased after 1 h [84].

It was intriguing, however, that the co-localization of LysoTracker® Red and HighcRGD-usGNP was only partial at any time point, which suggested a dynamic process in which the lysosomes constitute a stage only. We attempted to follow the usGNPs outside the lysosomes by labeling endosomal compartments with antibodies against their respective specific markers [10]. Anti-EEA1 antibody was used for labeling early endosomes, anti-RAB7 for late endosomes, and anti-RAB11 for recycling endosomes. In addition, an anti-RCAS1 antibody was used to label the Golgi compartment. Unfortunately, we found that the usGNPs leached out of the cells during permeabilization that was included to enable diffusion of the antibody into fixed cells (data not shown). Wu and co-workers successfully used co-staining of their 15 and 20 nm GNPs with antibodies on fixed cells with a similar methodology [85]. Our unsuccessful attempt to co-stain the usGNPs with antibodies likely reflects the 4 nm size of the usGNP core, which is smaller than the size of the antibodies [86].

### 3.6. Dual-Functionalized usGNPs Show Selective Cytotoxicity on $\alpha V\beta 3$ Integrin Expressing Cells

Lastly, we tested the ability of our functionalized usGNPs to deliver cytotoxic payload preferentially to  $\alpha V\beta 3$  expressing cells. Cytotoxicity of DM1 functionalized base usGNPs and LowcRGD-usGNPs was compared to DM1 alone on U-87 MG and Hep3B cells that do not express  $\alpha V\beta 3$  integrin [87]. usGNPs without DM1 were not cytotoxic over the same concentration range used for the functionalized usGNPs in either cell line (data not shown). For the Hep3B cell line, the cytotoxicity of DM1 was significantly reduced by the attachment to the usGNPs, presumably due to the rate of drug release from the usGNP. This is shown as an increase in the IC<sub>50</sub> value from 3.2 nM (95% CI: 2.4–4.7 nM) for free DM1, to 30.1 nM (95% CI: 25–36.3 nM) equivalent concentration for DM1-loaded usGNP (Figure 8a). Functionalization of the DM1-usGNP with the cRGD peptide did not significantly alter the cytotoxicity of the particle in Hep3B cells (IC<sub>50</sub>: 30.4 nM; 95% CI: 26.8–34.5 nM). However, for the  $\alpha V\beta 3$  integrin expressing U-87 MG cell line (Figure 8b), cRGD functionalization of DM1-LowcRGD-usGNPs improved targeted cytotoxicity of the nanoparticle compared to DM1-usGNPs, reducing the IC<sub>50</sub> value from 25.2 nM (95% CI: 21.5–29.7 nM) to 5 nM (95% CI: 4.2–5.9 nM) DM1 equivalent concentration, which is comparable to that of free DM1 in Hep3B cells and only moderately higher than the IC<sub>50</sub> of free DM1 (1.4 nM; 95% CI: 1.2–1.6 nM) in U-87 MG cells. These data indicate that the presence of the cRGD peptide can be used to selectively target a DM1-loaded usGNP for cells expressing the  $\alpha V\beta 3$  integrin, providing a mechanism for the selective killing of cells and reducing off-target effects.

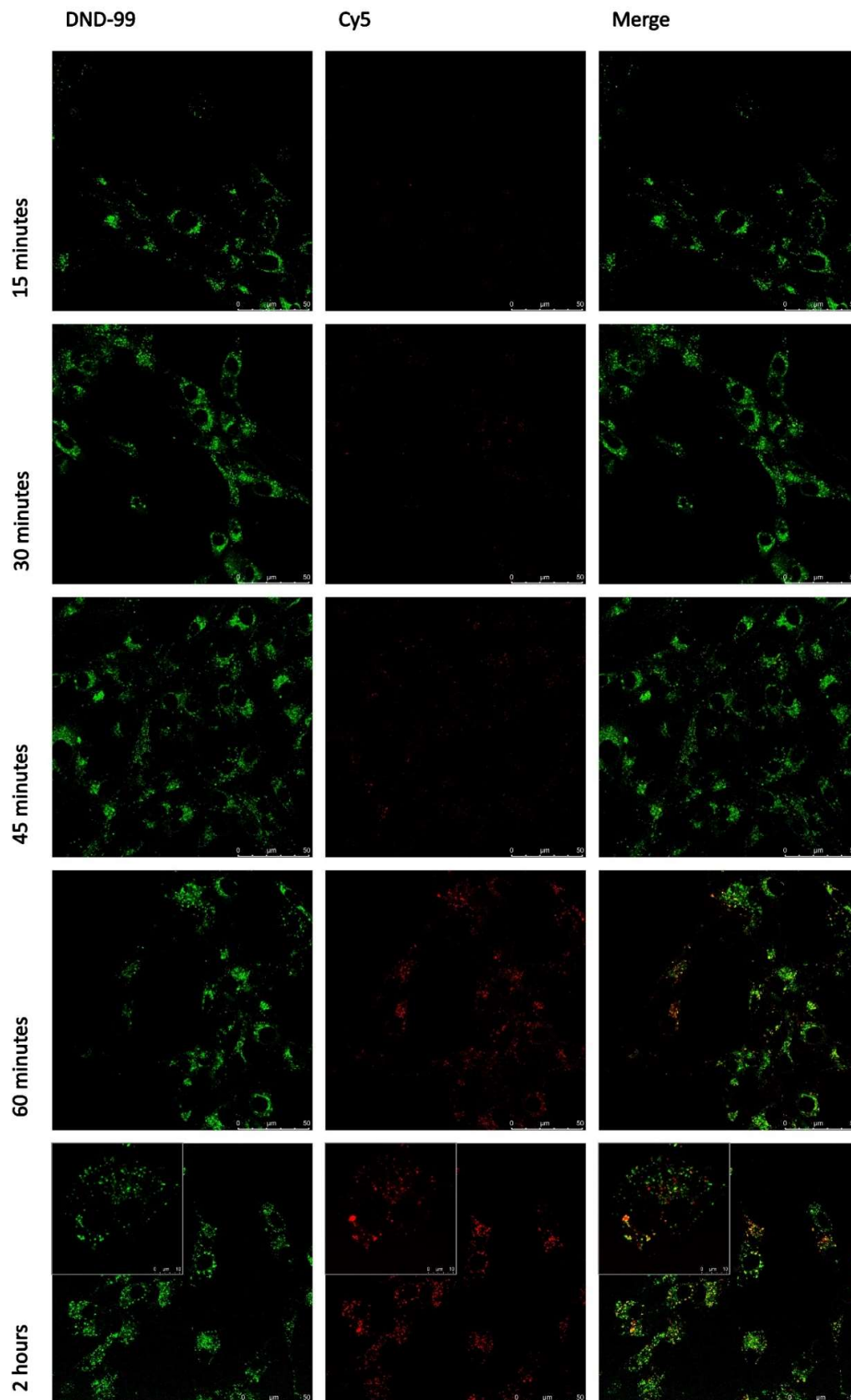


**Figure 7.** HighCRGD-usGNPs accumulate in the lysosomes. U-87 MG cells were incubated with HighCRGD-usGNPs at 9 nM final concentration for the indicated period. Fifteen minutes before

acquisition 1:100 LysoTracker<sup>®</sup> Red was added. Live cell images were taken with filter settings optimized for DND-99 (LysoTracker<sup>®</sup> Red, pseudo-colored green) and Cy5 (High-cRGD-usGNPs, red). The usGNPs appear co-localizing with the lysosomes after 30 min of incubation and reached a maximum after 2 h. Insets within the 2 h images show cells with a 3.5× zoom factor to better aid the comparison of co-localizing lysosomal and nanoparticle-derived signals.

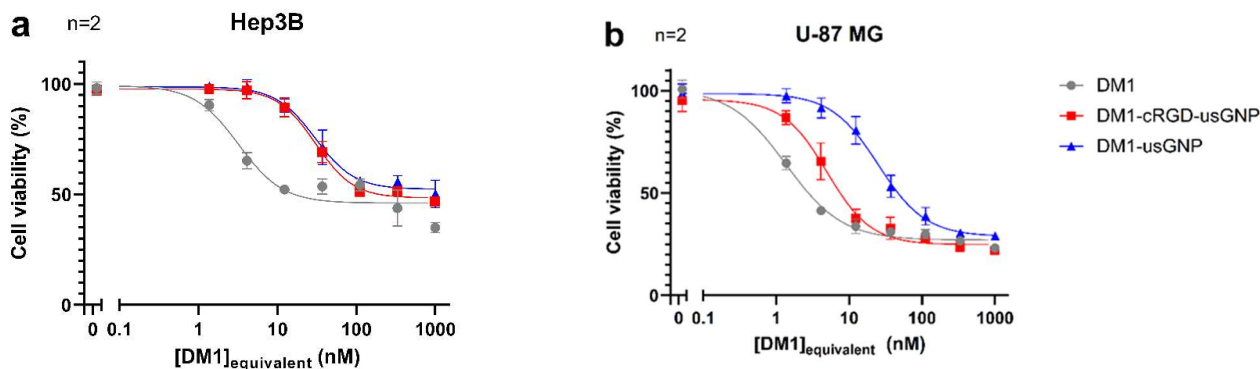


**Figure 8.** The presence of cRGD on usGNPs can selectively target  $\alpha V\beta 3$  integrin expressing cells with cytotoxic DM1 payload.  $\alpha V\beta 3$  integrin negative Hep3B (a) and positive U-87 MG (b) cells were treated with increasing concentrations of free DM1 (grey lines), DM1-functionalised base usGNP (blue) and DM1-LowcRGD-usGNPs (red). The presence of the cRGD ligand had no effect on the cytotoxicity of DM1 functionalized usGNPs in Hep3B cells. In U-87 MG cells, the cRGD sidechain increased cytotoxicity of DM1-LowcRGD-usGNPs nearly to the level of free DM1 confirming selective delivery of cytotoxic payload. Error bars represent SD of n independent experiments.

#### 4. Conclusions

Targeted delivery of cytotoxic drugs increases the therapeutic window by improving biodistribution, preventing off-target effects, or reducing drug degradation and elimination. Ultrasmall gold nanoparticles offer an improved surface-to-volume ratio that allows the immobilization of a larger number of different ligands at the same dose of gold, which presents an ideal platform for multiple functionalizations. Our strategy to link cRGD sidechains to the usGNP core via PEG(8)COOH lead to the successful binding of the functionalized usGNP to  $\alpha V\beta 3$  integrin both in vitro and in cell culture. This binding was selective and specifically proven by competition with free cRGD, functionalization with the non-interacting cRAD peptide, or using cell lines that do not express the  $\alpha V\beta 3$  integrin. The potential for multiple functionalization was shown by coupling fluorescent moieties to the usGNPs via the same PEG(8)COOH bridge, which permitted direct visualization of the usGNPs with confocal microscopy and monitoring their uptake and intracellular localization. Loading the maytansinoid drug DM1 onto the cRGD-usGNPs led to an improvement in selective toxicity on cells that express  $\alpha V\beta 3$  integrin and proved the potential of multi-functionalized usGNPs in improving the therapeutic window.

**Supplementary Materials:** The following supporting information can be downloaded at: <https://www.mdpi.com/article/10.3390/nano12224013/s1>, Figure S1: <sup>1</sup>H NMR (500 MHz, D<sub>2</sub>O,  $\delta$ ) of Base usGNP and cRGD-usGNP; Figure S2: LC-CAD chromatogram with MS assignation of Base GNP, cRGD-GNP, and Cy5-GNP; Figure S3: HPLC-UV chromatograms ( $\lambda$  276 nm) of DM1-usGNP after particle etching and ligand release; Figure S4: Verification of  $\alpha V\beta 3$  integrin expression in the cell lines employed.; Figure S5: A simplified representation of the clathrin-dependent and -independent mechanisms of endocytosis and their inhibitors.; Figure S6: Elevated concentrations of chlorpromazine hydrochloride cause cytotoxicity in U-87 MG cells.

**Author Contributions:** Investigation, L.-A.M., A.R., K.L.S., V.C., A.F., C.E.G., M.Á.R., D.L., I.P. and A.P.; Formal analysis, L.-A.M., A.R., V.C., A.F., R.D.P., E.F. and C.Z.B.; Methodology, L.-A.M., A.R., R.D.P., E.F., C.Z.B., A.P. and S.J.M.H.; Validation, L.-A.M., A.R., R.D.P., C.Z.B., V.C. and A.F.;

writing—draft, R.D.P., C.Z.B., V.C. and K.C.; writing—review and editing, C.Z.B., V.C., K.C., A.F. and E.F.; Visualization, C.Z.B., V.C., E.F., L.-A.M. and S.J.M.H.; Data curation, C.Z.B., V.C. and K.C.; Conceptualization, C.Z.B., K.C., E.F., S.J.M.H., J.P., A.B. and T.C.; Supervision, C.Z.B., K.C., E.F., S.J.M.H., J.P., A.B. and T.C.; Project administration, C.Z.B., K.C., S.J.M.H., J.P., A.B. and T.C.; Resources, C.Z.B., K.C., A.B. and T.C. All authors have read and agreed to the published version of the manuscript.

**Funding:** This project has received funding from the European Union’s Horizon 2020 research and innovation programs under the Marie Skłodowska-Curie grant agreements IMMUNOSHAPE 642870 for Valentin Cognet and NanoCarb 814236 for Avelino Ferreira. European Training Networks were co-supervised by Midatech Pharma España, Universidad del País Vasco (UPV/EHU), Barrio Sarriena, s/n, 48940 Leioa, Spain for the former and Department of Chemistry, Royal College of Surgeons in Ireland (RCSI), Dublin 2, Ireland for the latter.

**Institutional Review Board Statement:** The authors state that they have obtained a favorable opinion from the University of Lincoln Research Ethics Committee under project number 2018-Oct-0098 for the research described.

**Informed Consent Statement:** Not Applicable.

**Data Availability Statement:** The data presented in this study are available on request from the corresponding author.

**Acknowledgments:** The authors would like to thank Gail Calvert, Sartorius (FortéBio, Sartorius) for help in setting up the initial biotin-cRGD Integrin binding experiment; and Daniel Padro and Marco Möller from the Nuclear Magnetic Resonance and Electron Microscopy Platforms, respectively at CIC biomaGUNE, Parque Tecnológico de Gipuzkoa Ed. Pº Miramón 182, 20014, San Sebastián.

**Conflicts of Interest:** The authors declare no conflict of interest. The funders had no role in the design of the study; in the collection, analyses, or interpretation of data; in the writing of the manuscript; or in the decision to publish the results.

## References

1. Sperling, R.A.; Parak, W.J. Surface modification, functionalization and bioconjugation of colloidal inorganic nanoparticles. *Philos. Trans. A Math. Phys. Eng. Sci.* **2010**, *368*, 1333–1383. [[CrossRef](#)] [[PubMed](#)]
2. Conde, J.; Dias, J.T.; Grazu, V.; Moros, M.; Baptista, P.V.; de la Fuente, J.M. Revisiting 30 years of biofunctionalization and surface chemistry of inorganic nanoparticles for nanomedicine. *Front. Chem.* **2014**, *2*, 48. [[CrossRef](#)] [[PubMed](#)]
3. Arvizo, R.; Bhattacharya, R.; Mukherjee, P. Gold nanoparticles: Opportunities and challenges in nanomedicine. *Expert Opin. Drug Deliv.* **2010**, *7*, 753–763. [[CrossRef](#)] [[PubMed](#)]
4. Gilad, Y.; Noy, E.; Senderowitz, H.; Albeck, A.; Firer, M.A.; Gellerman, G. Dual-drug RGD conjugates provide enhanced cytotoxicity to melanoma and non-small lung cancer cells. *Biopolymers* **2016**, *106*, 160–171. [[CrossRef](#)] [[PubMed](#)]
5. Zhang, D.Y.; Zheng, Y.; Zhang, H.; Sun, J.H.; Tan, C.P.; He, L.; Zhang, W.; Ji, L.N.; Mao, Z.W. Delivery of Phosphorescent Anticancer Iridium(III) Complexes by Polydopamine Nanoparticles for Targeted Combined Photothermal-Chemotherapy and Thermal/Photoacoustic/Lifetime Imaging. *Adv. Sci.* **2018**, *5*, 1800581. [[CrossRef](#)] [[PubMed](#)]
6. Kim, M.; Sahu, A.; Kim, G.B.; Nam, G.H.; Um, W.; Shin, S.J.; Jeong, Y.Y.; Kim, I.S.; Kim, K.; Kwon, I.C.; et al. Comparison of in vivo targeting ability between cRGD and collagen-targeting peptide conjugated nano-carriers for atherosclerosis. *J. Control Release* **2018**, *269*, 337–346. [[CrossRef](#)]
7. Liang, M.; Yan, M.; Lu, Y.; Chen, I.S. Retargeting vesicular stomatitis virus glycoprotein pseudotyped lentiviral vectors with enhanced stability by in situ synthesized polymer shell. *Hum. Gene Ther. Methods* **2013**, *24*, 11–18. [[CrossRef](#)]
8. Feng, G.; Liu, J.; Liu, R.; Mao, D.; Tomczak, N.; Liu, B. Ultrasmall Conjugated Polymer Nanoparticles with High Specificity for Targeted Cancer Cell Imaging. *Adv. Sci.* **2017**, *4*, 1600407. [[CrossRef](#)]
9. Humphries, J.D.; Byron, A.; Humphries, M.J. Integrin ligands at a glance. *J. Cell Sci.* **2006**, *119*, 3901–3903. [[CrossRef](#)]
10. Moreno-Layseca, P.; Icha, J.; Hamidi, H.; Ivaska, J. Integrin trafficking in cells and tissues. *Nat. Cell Biol.* **2019**, *21*, 122–132. [[CrossRef](#)]
11. Li, K.; Zhang, Z.; Zheng, L.; Liu, H.; Wei, W.; Li, Z.; He, Z.; Larson, A.C.; Zhang, G. Arg-Gly-Asp-D-Phe-Lys peptide-modified PE-Gylated dendrimer-entrapped gold nanoparticles for targeted computed tomography imaging of breast carcinoma. *Nanomedicine* **2015**, *10*, 2185–2197. [[CrossRef](#)] [[PubMed](#)]
12. Morales-Avila, E.; Ferro-Flores, G.; Ocampo-Garcia, B.E.; De Leon-Rodriguez, L.M.; Santos-Cuevas, C.L.; Garcia-Becerra, R.; Medina, L.A.; Gomez-Olivan, L. Multimeric system of 99mTc-labeled gold nanoparticles conjugated to c[RGDfK(C)] for molecular imaging of tumor alpha(v)beta(3) expression. *Bioconjugate Chem.* **2011**, *22*, 913–922. [[CrossRef](#)] [[PubMed](#)]



13. Kim, Y.H.; Jeon, J.; Hong, S.H.; Rhim, W.K.; Lee, Y.S.; Youn, H.; Chung, J.K.; Lee, M.C.; Lee, D.S.; Kang, K.W.; et al. Tumor targeting and imaging using cyclic RGD-PEGylated gold nanoparticle probes with directly conjugated iodine-125. *Small* **2011**, *7*, 2052–2060. [[CrossRef](#)] [[PubMed](#)]
14. Su, N.; Dang, Y.; Liang, G.; Liu, G. Iodine-125-labeled cRGD-gold nanoparticles as tumor-targeted radiosensitizer and imaging agent. *Nanoscale Res. Lett.* **2015**, *10*, 160. [[CrossRef](#)] [[PubMed](#)]
15. Yu, Y.; Yang, T.; Sun, T. New insights into the synthesis, toxicity and applications of gold nanoparticles in CT imaging and treatment of cancer. *Nanomedicine* **2020**, *15*, 1127–1145. [[CrossRef](#)] [[PubMed](#)]
16. Yu, Y.; Wu, Y.; Liu, J.; Li, K.; Wu, D. Metabolizable dopamine-coated gold nanoparticle aggregates: Preparation, characteristics, computed tomography imaging, acute toxicity, and metabolism in vivo. *J. Mater. Chem. B Mater. Biol. Med.* **2016**, *4*, 1090–1099. [[CrossRef](#)]
17. Chen, Y.S.; Hung, Y.C.; Liao, I.; Huang, G.S. Assessment of the In Vivo Toxicity of Gold Nanoparticles. *Nanoscale Res. Lett.* **2009**, *4*, 858–864. [[CrossRef](#)]
18. Hale, S.J.M.; Perrins, R.D.; Garci, A.C.; Pace, A.; Peral, U.; Patel, K.R.; Robinson, A.; Williams, P.; Ding, Y.; Saito, G.; et al. DM1 Loaded Ultrasmall Gold Nanoparticles Display Significant Efficacy and Improved Tolerability in Murine Models of Hepatocellular Carcinoma. *Bioconjugate Chem.* **2019**, *30*, 703–713. [[CrossRef](#)]
19. Zhang, X.D.; Chen, J.; Luo, Z.; Wu, D.; Shen, X.; Song, S.S.; Sun, Y.M.; Liu, P.X.; Zhao, J.; Huo, S.; et al. Enhanced tumor accumulation of sub-2 nm gold nanoclusters for cancer radiation therapy. *Adv. Healthc. Mater.* **2014**, *3*, 133–141. [[CrossRef](#)]
20. Simpson, C.A.; Salleng, K.J.; Cliffl, D.E.; Feldheim, D.L. In vivo toxicity, biodistribution, and clearance of glutathione-coated gold nanoparticles. *Nanomedicine* **2013**, *9*, 257–263. [[CrossRef](#)]
21. Cho, W.S.; Cho, M.; Jeong, J.; Choi, M.; Cho, H.Y.; Han, B.S.; Kim, S.H.; Kim, H.O.; Lim, Y.T.; Chung, B.H.; et al. Acute toxicity and pharmacokinetics of 13 nm-sized PEG-coated gold nanoparticles. *Toxicol. Appl. Pharmacol.* **2009**, *236*, 16–24. [[CrossRef](#)] [[PubMed](#)]
22. Zhang, G.; Yang, Z.; Lu, W.; Zhang, R.; Huang, Q.; Tian, M.; Li, L.; Liang, D.; Li, C. Influence of anchoring ligands and particle size on the colloidal stability and in vivo biodistribution of polyethylene glycol-coated gold nanoparticles in tumor-xenografted mice. *Biomaterials* **2009**, *30*, 1928–1936. [[CrossRef](#)] [[PubMed](#)]
23. Schaeublin, N.M.; Braydich-Stolle, L.K.; Schrand, A.M.; Miller, J.M.; Hutchison, J.; Schlager, J.J.; Hussain, S.M. Surface charge of gold nanoparticles mediates mechanism of toxicity. *Nanoscale* **2011**, *3*, 410–420. [[CrossRef](#)]
24. Vales, G.; Suhonen, S.; Siivola, K.M.; Savolainen, K.M.; Catalán, J.; Norppa, H. Genotoxicity and Cytotoxicity of Gold Nanoparticles In Vitro: Role of Surface Functionalization and Particle Size. *Nanomaterials* **2020**, *10*, 271. [[CrossRef](#)] [[PubMed](#)]
25. Chandran, P.; Riviere, J.E.; Monteiro-Riviere, N.A. Surface chemistry of gold nanoparticles determines the biocorona composition impacting cellular uptake, toxicity and gene expression profiles in human endothelial cells. *Nanotoxicology* **2017**, *11*, 507–519. [[CrossRef](#)] [[PubMed](#)]
26. Vetten, M.; Gulumian, M. Differences in uptake of 14nm PEG-liganded gold nanoparticles into BEAS-2B cells is dependent on their functional groups. *Toxicol. Appl. Pharmacol.* **2019**, *363*, 131–141. [[CrossRef](#)]
27. Liu, J.; Yu, M.; Zhou, C.; Yang, S.; Ning, X.; Zheng, J. Passive tumor targeting of renal-clearable luminescent gold nanoparticles: Long tumor retention and fast normal tissue clearance. *J. Am. Chem. Soc.* **2013**, *135*, 4978–4981. [[CrossRef](#)]
28. Huang, K.; Ma, H.; Liu, J.; Huo, S.; Kumar, A.; Wei, T.; Zhang, X.; Jin, S.; Gan, Y.; Wang, P.C.; et al. Size-dependent localization and penetration of ultrasmall gold nanoparticles in cancer cells, multicellular spheroids, and tumors in vivo. *ACS Nano* **2012**, *6*, 4483–4493. [[CrossRef](#)]
29. Dykman, L.; Khlebtsov, N. Gold nanoparticles in biomedical applications: Recent advances and perspectives. *Chem. Soc. Rev.* **2012**, *41*, 2256–2282. [[CrossRef](#)]
30. Li, J.; Wang, X.; Wang, C.; Chen, B.; Dai, Y.; Zhang, R.; Song, M.; Lv, G.; Fu, D. The enhancement effect of gold nanoparticles in drug delivery and as biomarkers of drug-resistant cancer cells. *ChemMedChem* **2007**, *2*, 374–378. [[CrossRef](#)]
31. Patra, C.R.; Bhattacharya, R.; Wang, E.; Katarya, A.; Lau, J.S.; Dutta, S.; Muders, M.; Wang, S.; Buhrow, S.A.; Safgren, S.L.; et al. Targeted delivery of gemcitabine to pancreatic adenocarcinoma using cetuximab as a targeting agent. *Cancer Res.* **2008**, *68*, 1970–1978. [[CrossRef](#)] [[PubMed](#)]
32. Podsiadlo, P.; Sinani, V.A.; Bahng, J.H.; Kam, N.W.; Lee, J.; Kotov, N.A. Gold nanoparticles enhance the anti-leukemia action of a 6-mercaptopurine chemotherapeutic agent. *Langmuir* **2008**, *24*, 568–574. [[CrossRef](#)] [[PubMed](#)]
33. Azzam, E.M.S.; Morsy, S.M.I. Enhancement of the Antitumour Activity for the Synthesised Dodecylcysteine Surfactant using Gold Nanoparticles. *J. Surfactants Deterg.* **2008**, *11*, 195–199. [[CrossRef](#)]
34. Agasti, S.S.; Chompoosor, A.; You, C.C.; Ghosh, P.; Kim, C.K.; Rotello, V.M. Photoregulated release of caged anticancer drugs from gold nanoparticles. *J. Am. Chem. Soc.* **2009**, *131*, 5728–5729. [[CrossRef](#)] [[PubMed](#)]
35. Shi, Y.; Goodisman, J.; Dabrowiak, J.C. Cyclodextrin capped gold nanoparticles as a delivery vehicle for a prodrug of cisplatin. *Inorg. Chem.* **2013**, *52*, 9418–9426. [[CrossRef](#)] [[PubMed](#)]
36. Patra, C.R.; Bhattacharya, R.; Mukherjee, P. Fabrication and functional characterization of goldnanoconjugates for potential application in ovarian cancer. *J. Mater. Chem.* **2010**, *20*, 547–554. [[CrossRef](#)]
37. Zhang, X.; Shastry, S.; Bradforth, S.E.; Nadeau, J.L. Nuclear uptake of ultrasmall gold-doxorubicin conjugates imaged by fluorescence lifetime imaging microscopy (FLIM) and electron microscopy. *Nanoscale* **2015**, *7*, 240–251. [[CrossRef](#)]
38. Xu, C.; Tung, G.A.; Sun, S. Size and Concentration Effect of Gold Nanoparticles on X-ray Attenuation As Measured on Computed Tomography. *Chem. Mater.* **2008**, *20*, 4167–4169. [[CrossRef](#)]

39. Tsvirkun, D.; Ben-Nun, Y.; Merquiol, E.; Zlotver, I.; Meir, K.; Weiss-Sadan, T.; Matok, I.; Popovtzer, R.; Blum, G. CT Imaging of Enzymatic Activity in Cancer Using Covalent Probes Reveal a Size-Dependent Pattern. *J. Am. Chem. Soc.* **2018**, *140*, 12010–12020. [[CrossRef](#)]
40. Huo, S.; Jin, S.; Ma, X.; Xue, X.; Yang, K.; Kumar, A.; Wang, P.C.; Zhang, J.; Hu, Z.; Liang, X.J. Ultrasmall gold nanoparticles as carriers for nucleus-based gene therapy due to size-dependent nuclear entry. *ACS Nano* **2014**, *8*, 5852–5862. [[CrossRef](#)]
41. Jiang, W.; Kim, B.Y.; Rutka, J.T.; Chan, W.C. Nanoparticle-mediated cellular response is size-dependent. *Nat. Nanotechnol.* **2008**, *3*, 145–150. [[CrossRef](#)] [[PubMed](#)]
42. Hong, R.; Han, G.; Fernandez, J.M.; Kim, B.J.; Forbes, N.S.; Rotello, V.M. Glutathione-mediated delivery and release using monolayer protected nanoparticle carriers. *J. Am. Chem. Soc.* **2006**, *128*, 1078–1079. [[CrossRef](#)] [[PubMed](#)]
43. Lambert, J.M.; Morris, C.Q. Antibody-Drug Conjugates (ADCs) for Personalized Treatment of Solid Tumors: A Review. *Adv. Ther.* **2017**, *34*, 1015–1035. [[CrossRef](#)] [[PubMed](#)]
44. Bartczak, D.; Kanaras, A.G. Preparation of peptide-functionalized gold nanoparticles using one pot EDC/sulfo-NHS coupling. *Langmuir* **2011**, *27*, 10119–10123. [[CrossRef](#)]
45. Concepcion, J.; Witte, K.; Wartchow, C.; Choo, S.; Yao, D.; Persson, H.; Wei, J.; Li, P.; Heidecker, B.; Ma, W.; et al. Label-free detection of biomolecular interactions using BioLayer interferometry for kinetic characterization. *Comb. Chem. High Throughput Screen.* **2009**, *12*, 791–800. [[CrossRef](#)]
46. Allen, M.; Bjerke, M.; Edlund, H.; Neland, S.; Westermark, B. Origin of the U87MG glioma cell line: Good news and bad news. *Sci. Transl. Med.* **2016**, *8*, 354re3. [[CrossRef](#)]
47. McCarthy, L.A.; Dye, A.; Ferrari, E. Absolute Quantification of Gold Nanoparticles with Femtomolar Accuracy Using Inductively Coupled Plasma Atomic Emission Spectroscopy. *Methods Mol. Biol.* **2020**, *2118*, 283–288. [[CrossRef](#)]
48. Berridge, M.V.; Herst, P.M.; Tan, A.S. Tetrazolium dyes as tools in cell biology: New insights into their cellular reduction. *Biotechnol. Annu. Rev.* **2005**, *11*, 127–152. [[CrossRef](#)]
49. Brust, M.; Fink, J.; Bethell, D.; Schiffrin, D.J.; Kiely, C. Synthesis and reactions of functionalised gold nanoparticles. *J. Chem. Soc. Chem. Commun.* **1995**, *16*, 1655–1656. [[CrossRef](#)]
50. de la Fuente, J.M.; Barrientos, A.G.; Rojas, T.C.; Rojo, J.; Cañada, J.; Fernández, A.; Penadés, S. Gold Glyconanoparticles as Water-Soluble Polyvalent Models To Study Carbohydrate Interactions. *Angew. Chem. Int. Ed.* **2001**, *40*, 2257–2261. [[CrossRef](#)]
51. Hussain, I.; Graham, S.; Wang, Z.; Tan, B.; Sherrington, D.C.; Rannard, S.P.; Cooper, A.I.; Brust, M. Size-controlled synthesis of near-monodisperse gold nanoparticles in the 1–4 nm range using polymeric stabilizers. *J. Am. Chem. Soc.* **2005**, *127*, 16398–16399. [[CrossRef](#)] [[PubMed](#)]
52. Roskamp, M.; Coulter, T.; Ding, Y.; Perrins, R.; Espinosa Garcia, C.; Pace, A.; Hale, S.; Robinson, A.; Williams, P.; Aguilera Peral, U.; et al. SIKVAV peptide functionalized ultra-small gold nanoparticles for selective targeting of  $\alpha\beta 1$  integrin in hepatocellular carcinoma. *J. Phys. Conf. Ser.* **2017**, *829*, 012017. [[CrossRef](#)]
53. Arosio, D.; Manzoni, L.; Araldi, E.M.; Scolastico, C. Cyclic RGD functionalized gold nanoparticles for tumor targeting. *Bioconjugate Chem.* **2011**, *22*, 664–672. [[CrossRef](#)] [[PubMed](#)]
54. Kang, B.; Opatz, T.; Landfester, K.; Wurm, F.R. Carbohydrate nanocarriers in biomedical applications: Functionalization and construction. *Chem. Soc. Rev.* **2015**, *44*, 8301–8325. [[CrossRef](#)] [[PubMed](#)]
55. Charbgoon, F.; Nejabat, M.; Abnous, K.; Soltani, F.; Taghdisi, S.M.; Alibolandi, M.; Thomas Shier, W.; Steele, T.W.J.; Ramezani, M. Gold nanoparticle should understand protein corona for being a clinical nanomaterial. *J. Control Release* **2018**, *272*, 39–53. [[CrossRef](#)]
56. Manson, J.; Kumar, D.; Meenan, B.J.; Dixon, D. Polyethylene glycol functionalized gold nanoparticles: The influence of capping density on stability in various media. *Gold Bull.* **2011**, *44*, 99–105. [[CrossRef](#)]
57. Alalaiwe, A.; Roberts, G.; Carpinone, P.; Munson, J.; Roberts, S. Influence of PEG coating on the oral bioavailability of gold nanoparticles in rats. *Drug Deliv.* **2017**, *24*, 591–598. [[CrossRef](#)]
58. Vergara, S.; Santiago, U.; Kumara, C.; Alducin, D.; Whetten, R.L.; Jose Yacaman, M.; Dass, A.; Ponce, A. Synthesis, Mass Spectrometry, and Atomic Structural Analysis of Au~2000(SR)~290 Nanoparticles. *J. Phys. Chem. A* **2018**, *122*, 26733–26738. [[CrossRef](#)]
59. Goutayer, M.; Dufort, S.; Josserand, V.; Royere, A.; Heinrich, E.; Vinet, F.; Bibette, J.; Coll, J.L.; Texier, I. Tumor targeting of functionalized lipid nanoparticles: Assessment by in vivo fluorescence imaging. *Eur. J. Pharm. Biopharm.* **2010**, *75*, 137–147. [[CrossRef](#)]
60. Neiryneck, P.; Brinkmann, J.; An, Q.; van der Schaft, D.W.; Milroy, L.G.; Jonkheijm, P.; Brunsveld, L. Supramolecular control of cell adhesion via ferrocene-cucurbit[7]uril host-guest binding on gold surfaces. *Chem. Commun.* **2013**, *49*, 3679–3681. [[CrossRef](#)]
61. Algar, W.R.; Prasuhan, D.E.; Stewart, M.H.; Jennings, T.L.; Blanco-Canosa, J.B.; Dawson, P.E.; Medintz, I.L. The controlled display of biomolecules on nanoparticles: A challenge suited to bioorthogonal chemistry. *Bioconjugate Chem.* **2011**, *22*, 825–858. [[CrossRef](#)] [[PubMed](#)]
62. Wu, R.H.; Nguyen, T.P.; Marquart, G.W.; Miesen, T.J.; Mau, T.; Mackiewicz, M.R. A facile route to tailoring peptide-stabilized gold nanoparticles using glutathione as a synthon. *Molecules* **2014**, *19*, 6754–6775. [[CrossRef](#)] [[PubMed](#)]
63. Hostetler, M.J.; Templeton, A.C.; Murray, R.W. Dynamics of Place-Exchange Reactions on Monolayer-Protected Gold Cluster Molecules. *Langmuir* **1999**, *15*, 3782–3789. [[CrossRef](#)]

64. Schulz, F.; Vossmeier, T.; Bastus, N.G.; Weller, H. Effect of the spacer structure on the stability of gold nanoparticles functionalized with monodentate thiolated poly(ethylene glycol) ligands. *Langmuir* **2013**, *29*, 9897–9908. [[CrossRef](#)] [[PubMed](#)]
65. Templeton, A.C.; Hostetler, M.J.; Kraft, C.T.; Murray, R.W. Reactivity of Monolayer-Protected Gold Cluster Molecules: Steric Effects. *J. Am. Chem. Soc.* **1998**, *120*, 1906–1911. [[CrossRef](#)]
66. Smith, M.C.; Crist, R.M.; Clogston, J.D.; McNeil, S.E. Quantitative analysis of PEG-functionalized colloidal gold nanoparticles using charged aerosol detection. *Anal. Bioanal. Chem.* **2015**, *407*, 3705–3716. [[CrossRef](#)] [[PubMed](#)]
67. Robinson, M.W.; Hill, A.P.; Readshaw, S.A.; Hollerton, J.C.; Upton, R.J.; Lynn, S.M.; Besley, S.C.; Boughtflower, B.J. Use of Calculated Physicochemical Properties to Enhance Quantitative Response When Using Charged Aerosol Detection. *Anal. Chem.* **2017**, *89*, 1772–1777. [[CrossRef](#)]
68. Kirchofer, D.; Grzesiak, J.; Pierschbacher, M.D. Calcium as a potential physiological regulator of integrin-mediated cell adhesion. *J. Biol. Chem.* **1991**, *266*, 4471–4477. [[CrossRef](#)]
69. Paramanathan, T.; Reeves, D.; Friedman, L.J.; Kondev, J.; Gelles, J. A general mechanism for competitor-induced dissociation of molecular complexes. *Nat. Commun.* **2014**, *5*, 5207. [[CrossRef](#)]
70. Cui, Y.; Song, X.; Li, S.; He, B.; Yuan, L.; Dai, W.; Zhang, H.; Wang, X.; Yang, B.; Zhang, Q. The impact of receptor recycling on the exocytosis of alphavbeta3 integrin targeted gold nanoparticles. *Oncotarget* **2017**, *8*, 38618–38630. [[CrossRef](#)]
71. Benedetto, S.; Pulito, R.; Crich, S.G.; Tarone, G.; Aime, S.; Silengo, L.; Hamm, J. Quantification of the expression level of integrin receptor alpha(v)beta3 in cell lines and MR imaging with antibody-coated iron oxide particles. *Magn. Reson. Med.* **2006**, *56*, 711–716. [[CrossRef](#)] [[PubMed](#)]
72. Kang, W.; Svirskis, D.; Sarojini, V.; McGregor, A.L.; Bevitt, J.; Wu, Z. Cyclic-RGDyC functionalized liposomes for dual-targeting of tumor vasculature and cancer cells in glioblastoma: An in vitro boron neutron capture therapy study. *Oncotarget* **2017**, *8*, 36614–36627. [[CrossRef](#)] [[PubMed](#)]
73. Wang, T.; Li, G.; Wang, D.; Li, F.; Men, D.; Hu, T.; Xi, Y.; Zhang, X.E. Quantitative profiling of integrin alphavbeta3 on single cells with quantum dot labeling to reveal the phenotypic heterogeneity of glioblastoma. *Nanoscale* **2019**, *11*, 18224–18231. [[CrossRef](#)] [[PubMed](#)]
74. Shaw, S.K.; Schreiber, C.L.; Roland, F.M.; Battles, P.M.; Brennan, S.P.; Padanilam, S.J.; Smith, B.D. High expression of integrin alphavbeta3 enables uptake of targeted fluorescent probes into ovarian cancer cells and tumors. *Bioorganic Med. Chem.* **2018**, *26*, 2085–2091. [[CrossRef](#)]
75. Kok, R.J.; Schraa, A.J.; Bos, E.J.; Moorlag, H.E.; Asgeirsdottir, S.A.; Everts, M.; Meijer, D.K.; Molema, G. Preparation and functional evaluation of RGD-modified proteins as alpha(v)beta(3) integrin directed therapeutics. *Bioconjugate Chem.* **2002**, *13*, 128–135. [[CrossRef](#)]
76. Morlieras, J.; Dufort, S.; Sancey, L.; Truillet, C.; Mignot, A.; Rossetti, F.; Dentamaro, M.; Laurent, S.; Vander Elst, L.; Muller, R.N.; et al. Functionalization of small rigid platforms with cyclic RGD peptides for targeting tumors overexpressing alphavbeta3-integrins. *Bioconjugate Chem.* **2013**, *24*, 1584–1597. [[CrossRef](#)]
77. Taherian, A.; Li, X.; Liu, Y.; Haas, T.A. Differences in integrin expression and signaling within human breast cancer cells. *BMC Cancer* **2011**, *11*, 293. [[CrossRef](#)]
78. Zuidema, A.; Wang, W.; Kreft, M.; Te Molder, L.; Hoekman, L.; Bleijerveld, O.B.; Nahidiazar, L.; Janssen, H.; Sonnenberg, A. Mechanisms of integrin alphaVbeta5 clustering in flat clathrin lattices. *J. Cell Sci.* **2018**, *131*, jcs221317. [[CrossRef](#)]
79. Brassard, D.L.; Maxwell, E.; Malkowski, M.; Nagabhushan, T.L.; Kumar, C.C.; Armstrong, L. Integrin alpha(v)beta(3)-mediated activation of apoptosis. *Exp. Cell Res.* **1999**, *251*, 33–45. [[CrossRef](#)]
80. Puri, V.; Watanabe, R.; Singh, R.D.; Dominguez, M.; Brown, J.C.; Wheatley, C.L.; Marks, D.L.; Pagano, R.E. Clathrin-dependent and -independent internalization of plasma membrane sphingolipids initiates two Golgi targeting pathways. *J. Cell Biol.* **2001**, *154*, 535–547. [[CrossRef](#)]
81. Francia, V.; Reker-Smit, C.; Boel, G.; Salvati, A. Limits and challenges in using transport inhibitors to characterize how nano-sized drug carriers enter cells. *Nanomedicine* **2019**, *14*, 1533–1549. [[CrossRef](#)] [[PubMed](#)]
82. dos Santos, T.; Varela, J.; Lynch, I.; Salvati, A.; Dawson, K.A. Effects of transport inhibitors on the cellular uptake of carboxylated polystyrene nanoparticles in different cell lines. *PLoS ONE* **2011**, *6*, e24438. [[CrossRef](#)] [[PubMed](#)]
83. Xiao, Y.; Xu, W.; Komohara, Y.; Fujiwara, Y.; Hirose, H.; Futaki, S.; Niidome, T. Effect of Surface Modifications on Cellular Uptake of Gold Nanorods in Human Primary Cells and Established Cell Lines. *ACS Omega* **2020**, *5*, 32744–32752. [[CrossRef](#)] [[PubMed](#)]
84. Tsai, C.Y.; Lu, S.L.; Hu, C.W.; Yeh, C.S.; Lee, G.B.; Lei, H.Y. Size-dependent attenuation of TLR9 signaling by gold nanoparticles in macrophages. *J. Immunol.* **2012**, *188*, 68–76. [[CrossRef](#)]
85. Wu, P.H.; Onodera, Y.; Ichikawa, Y.; Rankin, E.B.; Giaccia, A.J.; Watanabe, Y.; Qian, W.; Hashimoto, T.; Shirato, H.; Nam, J.M. Targeting integrins with RGD-conjugated gold nanoparticles in radiotherapy decreases the invasive activity of breast cancer cells. *Int. J. Nanomed.* **2017**, *12*, 5069–5085. [[CrossRef](#)]
86. Tan, Y.H.; Liu, M.; Nolting, B.; Go, J.G.; Gervay-Hague, J.; Liu, G.Y. A nanoengineering approach for investigation and regulation of protein immobilization. *ACS Nano* **2008**, *2*, 2374–2384. [[CrossRef](#)]
87. Nejari, M.; Hafdi, Z.; Gouysse, G.; Fiorentino, M.; Beatrix, O.; Dumortier, J.; Pourreyron, C.; Barozzi, C.; D'Errico, A.; Grigioni, W.F.; et al. Expression, regulation, and function of alpha V integrins in hepatocellular carcinoma: An in vivo and in vitro study. *Hepatology* **2002**, *36*, 418–426. [[CrossRef](#)]